



**LIMITATIONS IN TIME RESOLVED PHOTOLUMINESCENCE OF GALLIUM
NITRIDE USING A STREAK CAMERA**

THESIS

Thomas R. Jost, Captain, USAF

AFIT/GAP/ENP/05-04

DEPARTMENT OF THE AIR FORCE
AIR UNIVERSITY

AIR FORCE INSTITUTE OF TECHNOLOGY

Wright-Patterson Air Force Base, Ohio

APPROVED FOR PUBLIC RELEASE; DISTRIBUTION UNLIMITED

The views expressed in this thesis are those of the author and do not reflect the official policy or position of the United States Air Force, Department of Defense, or the United States Government.

AFIT/GAP/ENP/05-04

LIMITATIONS IN TIME RESOLVED PHOTOLUMINESCENCE OF GALLIUM
NITRIDE USING A STREAK CAMERA

THESIS

Presented to the Faculty

Department of Engineering Physics

Graduate School of Engineering and Management

Air Force Institute of Technology

Air University

Air Education and Training Command

in Partial Fulfillment of the Requirements for the

Degree of Master of Science (Applied Physics)

Thomas R. Jost, BS

Captain, USAF

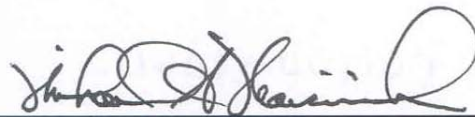
March 2005

APPROVED FOR PUBLIC RELEASE; DISTRIBUTION UNLIMITED

LIMITATIONS IN TIME RESOLVED PHOTOLUMINESCENCE OF GALLIUM
NITRIDE USING A STREAK CAMERA

Thomas R. Jost, BS
Captain, USAF

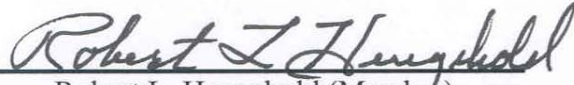
Approved:



Michael A. Marciniak (Chairman)

28 Feb 05

Date



Robert L. Hengehold (Member)

28 Feb 05

Date



David E. Weeks (Member)

28 Feb 05

Date

Abstract

Semiconductor performance is often characterized in terms of the rate at which its carrier recombination processes occur. Carrier recombination, including radiative, and Shockley-Read-Hall and Auger (both nonradiative), occurs at ultra-fast times in the picosecond or femtosecond regimes. A device which can measure both spectral data and temporal phenomena at this speed is the streak camera. The capability to do time-resolved spectroscopy of wide band gap semiconductors using a streak camera has been established at AFIT for the first time. Time resolved photoluminescence (TRPL) from samples of gallium nitride were measured at temperatures of 5 K over spectral bands of 36.6 Å and temporal ranges of 45 to 1970 ps, both instrument-limited. TRPL features at 3552 Å and 3587 Å were studied giving decay lifetimes of 43.2 ± 1.6 ps and 16.8 ± 3.4 ps, respectively. Shockley-Read-Hall, Radiative and Auger coefficients were found but parameterized in terms of experimental efficiency, η , which was not measured. These values, determined using a least-squares-error fit of the carrier recombination rate equation to collected data, are $-9.3 \times 10^9 \pm 4.9 \times 10^8 \text{ s}^{-1}$, $7.5 \times 10^{17} \eta \pm 8.0 \times 10^{16} \eta \text{ cm}^3/\text{s}$ and $1.8 \times 10^{25} \eta^2 \pm 2.9 \times 10^{24} \eta^2 \text{ cm}^6/\text{s}$, respectively, for the first peak and $-2.5 \times 10^{10} \pm 5.2 \times 10^9 \text{ s}^{-1}$, $4.9 \times 10^{19} \eta \pm 2.0 \times 10^{19} \eta \text{ cm}^3/\text{s}$ and $-1.4 \times 10^{28} \eta^2 \pm 8.6 \times 10^{27} \eta^2 \text{ cm}^6/\text{s}$ for the second peak. Since alignment of the streak camera has not yet been optimized, large but unquantified uncertainty in these results exists. Isolating vibrations and improving streak camera alignment should reduce the uncertainty and permit data collection temporally resolved at hundreds of femtoseconds.

AFIT/GAP/ENP/05-04

To my wife

Acknowledgments

When I met Dr. Hengehold in 1999, he gently challenged my undergraduate performance: “Why didn’t you live up to your potential?” Thank you for seeing the potential and agreeing that I qualified for AFIT. It gave me a new chance. Dr. Marciniak extended the opportunity with his contagious enthusiasm for this project. It feels like the result of my work is the smallest extension of what has already been done, but I hope it increases your enthusiasm for research prospects ahead. Technicians Mike and Greg kindly let me think this was “my” experiment, but your work truly set the timeline. Maj Webber sacrificially tutored me through the coursework and edited this thesis.

High school science teachers, Mrs. Parr and Mr. Hecht, and USAFA professor LtCol White taught me science, but more importantly, modeled a passion for learning it.

Mom and Dad, thank you for your constant love and support. I wish we weren’t so far away, and though our next assignment is exciting, it’s still further. I know—“I never had it so good.”

To my dear wife, you helped me through my masters program far more than I helped you through yours! Thank you for joining me in the adventure of life with its struggles and joys – especially for the little “bundle of joy” we expect later this year. Your love inspires me in ways that words can not express. I love you.

Finally, studying light reminds me of its Creator, Jesus Christ, who declared, “I am the light of the world; he who follows Me shall not walk in the darkness, but shall have the light of life” [John 8:12, NAS]. I owe all to You.

Thomas R. Jost

Table of Contents

	Page
Abstract.....	iv
Acknowledgments.....	vi
List of Figures	ix
List of Tables	xi
List of Abbreviations and Symbols.....	xii
 I. Introduction.....	 1
Background.....	1
Problem Statement	2
Research Objectives.....	2
Research Focus	2
Methodology	2
Implications.....	3
 II. Theoretical Background.....	 4
Characteristics of Semiconductors.....	4
Crystalline Structure.	4
Dispersion Relation.....	6
Energy Band Structure.....	8
Carrier Density	11
Effects of Impurities.	14
Effects of Temperature.	17
Effects of Temperature and Impurities.	20
Excitons.....	24
Carrier Recombination.....	25
Radiative Recombination.....	26
Non-radiative Recombination.	27
Carrier Recombination Rate	32
Time Resolved Photoluminescence	35
 III. Experimental Setup.....	 36
Time Resolved Photoluminescence Experiment	36
Laser System.....	38

Photoluminescence.	40
Light Measurement System: Streak Camera.....	41
New Equipment Setup	46
Equipment Installation and Integration.....	47
Troubleshooting.	48
IV. Experimental Data and Results	49
Overview	49
Spectrometer Data.....	49
Spectral Accuracy.	49
Spectral Resolution Versus Signal Strength.	50
Streak Camera Data	52
Spectral Data.	52
Temporal Data.	57
Semiconductor Data.....	63
Time-Integrated Photoluminescence.	63
Time-Resolved Photoluminescence.....	65
V. Conclusions and Recommendations	74
Conclusions about Experimental Setup	74
Conclusions about Samples	75
Recommendations.....	76
Major Recommendations to Laboratory Setup.	76
Minor Recommendations to Laboratory Setup.....	79
Recommendations for Further Research.....	80
Summary	81
Appendix A: Calibration of Streak Camera Wavelength	82
Overview	82
Calibration Procedure	82
Analysis.....	83
Bibliography	84
Vita.....	87

List of Figures

Figure	Page
1. Two Dimensional Crystalline Lattice Structure.	5
2. Merging of Electronic Orbitals.	6
3. Dispersion Relation for Periodic Potential of Crystalline Lattice.	7
4. Notional Diagram of Energy as a Function of Momentum.	10
5. Theoretical Carrier Densities.	12
6. Silicon Lattice with an Acceptor.....	14
7. Silicon Lattice with a Donor.	15
8. Increased Electron Density Due to the Presence of Donors.	16
9. Lattice Constants as a Function of Temperature for Wurtzite (Hexagonal) GaN. ..	18
10. Band Gap as a Function of Temperature.	18
11. Carrier Concentration Dependence on Impurity Concentration and Temperature..	21
12. Energy Levels of Excitons.	25
13. Types of Radiative Transitions.	27
14. Auger Processes.	31
15. Logarithmic/Linear Plot of Double Exponential Equation.....	35
16. Experimental Setup.....	37
17. Argon Ion Laser.	38
18. Titanium: Sapphire Laser.....	39
19. Third Harmonic Generator.....	39
20. Helitran.	40
21. Streak Camera Operation.....	42
22. Relationship between Sweep Voltage and Streak Camera Time Range.....	43

23.	Hamamatsu Synchroscan FESCA C6860.....	44
24.	Spectral Response of the Hamamatsu C6860 Streak Camera.	45
25.	Wavelength Error in Spectrometer.	50
26.	Mercury Doublet Resolved on Photomultiplier Tube (PMT).....	51
27.	Spectrometer Spectral Resolution versus Slit Widths.	51
28.	Spectrum from Mercury Doublet as Recorded on PMT.....	53
29.	Spectrum from Mercury Doublet as Recorded on Streak Camera.	53
30.	Mercury Doublet Image from Streak Camera Mapped to Spectrum.	54
31.	Streak Camera Spectral Resolution Versus Spectrometer Slit Width.	55
32.	Mercury Doublet Spectrum Resolved on Streak Camera.	56
33.	Temporal Resolution Dependence on Sweep Time Range and Spectrometer Slit Width.....	59
34.	Poorly Resolved Laser Pulses on All Temporal Time Ranges.	61
35.	TRPL of a Laser Pulse with Low Temporal Dispersion.....	62
36.	Pulse Widths of Laser Pulses Measured on the Streak Camera.....	62
37.	Time-Integrated Photoluminescence of GaN at 294 K.....	63
38.	Time-Integrated Photoluminescence of GaN at 5 K.....	64
39.	Streak Image of GaN at 5K.....	65
40.	Streak Camera Spectrum of GaN at 5 K Bounded on the PL Spectrum.....	66
41.	Temporal Profiles of TRPL Collected around 3552 Å.	67
42.	Double Exponential Curve Fits to Luminescence Intensity Decay Data.....	69
43.	Least Squares Error Fit to Luminescence Intensity Decay Data.	70
44.	Sequential TRPL Streaks of GaN at 5 K with Varied Sweep Delay.	73

List of Tables

Table	Page
1. Sweep Times for Time Range Control of the Streak Camera.	43
2. Map of Streak Camera to Spectrum.	55
3. Decay Times from Least-Squares Error Fit to a Double Exponential.	68
4. Parameters for Least Squares Error Fit to Luminescence Intensity Decay Data.	70
5. Values for A_{SRH} , B_{Rad} , C_{Aug} .	71

List of Abbreviations and Symbols

α	Absorption coefficient (cm^{-1})
A	Shockley-Read-Hall coefficient
\AA	Angstroms (10^{-10} m)
B	Radiative coefficient
BBO	beta barium borate
c	Speed of light
C	Auger coefficient
d	Diameter
Δ	Split-off band separation
Δn	Excess electrons
Δp	Excess holes
e	Electron
ϵ	Dielectric constant
ϵ	Energy (eV)
ϵ_A	Acceptor energy level (eV)
ϵ_C	Conduction band energy level (eV)
ϵ_D	Donor energy level (eV)
ϵ_f	Fermi energy level (eV)
ϵ_{fi}	Intrinsic Fermi energy (eV)
ϵ_g	Energy gap or band gap (eV)
ϵ_V	Valence band energy level (eV)
E_l	Laser energy (J)
$f(\epsilon)$	Fermi distribution
FWHM	Full width half maximum
$g(\epsilon)$	Density of states (cm^{-3})
h	Hole
h	Planck's constant
\hbar	Planck's constant divided by 2π
hh	Heavy hole
k	Wavenumber or spatial frequency (cm^{-1})
k_B	Boltzman's constant
l	Semiconductor thickness (cm)
lh	Light hole
L	Luminescence intensity (J/cm^2)
L'	Measured luminescence intensity (J/cm^2)
L_{bg}	Background luminescence (J/cm^2)
LBO	Lithium triborate
λ	Wavelength (\AA or nm)
m_0	Rest mass of the electron (kg)
m^*	Effective mass (kg)
m_e^*	Effective mass of the electron (kg)

m_{hh}^*	Effective mass of the heavy hole (kg)
m_{lh}^*	Effective mass of the light hole (kg)
m_{so}^*	Effective mass of the split-off hole (kg)
n	Negative charge carrier concentration (cm^{-3})
n	Principle quantum number
n_i	Intrinsic carrier concentration (cm^{-3})
n_0	Equilibrium density of electrons in the conduction band (cm^{-3})
ν	Frequency (Hz)
η	Experimental efficiency (unitless)
N_a	Acceptors concentration (cm^{-3})
N_c	Number of electrons in the conduction band
N_d	Donor concentration (cm^{-3})
N_v	Number of holes in the valence band
OPL	Optical Path Length
ω	Angular frequency (radians)
p	Momentum (kg m/s)
p	Positive charge carrier density (cm^{-3})
p_0	Equilibrium density of holes in the valence band (cm^{-3})
PL	Photoluminescence (time-integrated)
PMT	Photomultiplier tube
PRF	Pulse repetition frequency (Hz)
q	Fundamental charge
R	Carrier recombination rate (cm^3/s)
R_s	Surface reflection loss
σx	Uncertainty in x
so	Split-off or spin-orbit hole
SC	Streak Camera
t	Time (ps or fs)
τ	Time constant (ps)
T	Temperature (K)
THG	Third harmonic generator or third harmonic generation
TRPL	Time-resolved photoluminescence
V	Volume (cm^3)
w	Beam radius (cm)

LIMITATIONS IN TIME RESOLVED PHOTOLUMINESCENCE OF GALLIUM NITRIDE USING A STREAK CAMERA

I. Introduction

Background

We live in the Information Age, and information processing impacts virtually every aspect of our lives. Perhaps no other invention has so singularly ushered in this era as the integrated circuit inscribed on a semiconductor. Impact from semiconductors extends beyond computer processing as lasers made from semiconductors are also critical for information storage and retrieval on machines such as compact disk-read only memory (CD-ROM's) and digital video disks (DVD's). Advances in semiconductor technology will enable even more compact data storage.

Semiconductor devices are widely used both as optical and electronic devices in a wide variety of civilian and military applications. Regardless of the application, improving device performance requires an understanding of a phenomenon called carrier recombination. The rates at which different types of carrier recombination (radiative and non-radiative) occur determine the efficiency and utility of a device. The ability to measure these rates accurately is the first step to being able to engineer better devices.

Gallium nitride (GaN) has relatively new application as a semiconductor. Due to its wide band gap, it was formerly considered to be an insulator as it only absorbs light energy in the ultra-violet range. Its novelty means its properties are relatively unexplored

compared to better-known materials, and there is a need to determine what fabrication techniques result in the best materials.

Problem Statement

The goal of this research was to establish a laboratory experiment to perform both time-integrated photoluminescence (PL) and streak camera measurement of time-resolved photoluminescence (TRPL) from GaN carrier recombination events.

Research Objectives

Objective 1: Design, build and test an operational laboratory experiment which uses a streak camera to perform TRPL.

Objective 2: Collect PL and TRPL spectral data (check for self-consistency) and temporal TRPL data from carrier recombination events.

Objective 3: Calculate radiative, Shockley-Read-Hall and Auger coefficients for GaN samples.

Research Focus

Analysis of the TRPL data is expected to provide insight into the mechanisms of carrier recombination events.

Methodology

An ultra-short pulsed laser was used to stimulate GaN samples which will be held at temperatures as low as 5 K. The photoluminescence from the sample stimulation will be captured and spectrally dispersed into a photomultiplier tube for time-integrated

photoluminescence or alternatively into a streak camera for time-resolved photoluminescence. These data for each sample will be analyzed by fit to an integrated solution for the carrier recombination rate equation.

Implications

Carrier recombination characterization is applicable to any semiconductor sample, but only those with a band gap corresponding to light in the 200-850 nm regime may be measured with the current streak camera. Because the titanium: sapphire laser has a gain wavelength ranging from 700-1020 nm [1:392], it only overlaps the sensor region of the camera at the upper end. Semiconductors (such as GaN or SiC) with wide band gaps corresponding to wavelengths in the ultraviolet can be measured if the 810 nm peak wavelength is frequency-tripled to 270 nm.

When a laser is used to inscribe information on devices, such as CD-ROM's and DVD's, the amount of information that can be stored in a given area depends on the spot size of the laser. Minimal laser spot size is determined by a phenomenon called the diffraction limit, $1.22\lambda/d$ (where λ is the wavelength and d is the diffracting aperture's diameter) [2:224]. The wavelength dependence of the diffraction limit, stresses the importance of short wavelength sources when small beam size is a criteria. Advances in higher density (spatially compact) information storage will depend on our ability to produce these sources robustly and efficiently.

II. Theoretical Background

Characteristics of Semiconductors

Semiconductors are materials which are good conductors, but unlike metals which conduct only negative charge carriers (electrons), semiconductors conduct both positive charge carriers (holes) and negative charge carriers [3:372]. To understand semiconductor performance, it is important to understand the various physical characteristics which make them unique materials. These characteristics include crystalline structure, dispersion relationships and energy band structure.

Crystalline Structure.

A perfect semiconductor is an ideal crystalline solid which McKelvey defines as a substance with highly ordered periodic structure to its constituent atoms. Adjacent atoms are joined by tight covalent bonds and hence the atoms are very close together (1-2 Å). The location of the atoms in the periodic structure is known as the crystal lattice [3:4]. A notional two-dimensional crystal lattice structure is depicted in Figure 1. Although ideal crystals are as unachievable as the ideal gas, it is the simplest model and serves as a beginning point for all semiconductor analysis [3:373].

Crystalline structure allows for a very systematic analysis of the quantum mechanical interaction of the atoms. This analysis—called the Kronig-Penny model after R. de L. Kronig and G. Penney—predicts macroscopic results which are otherwise

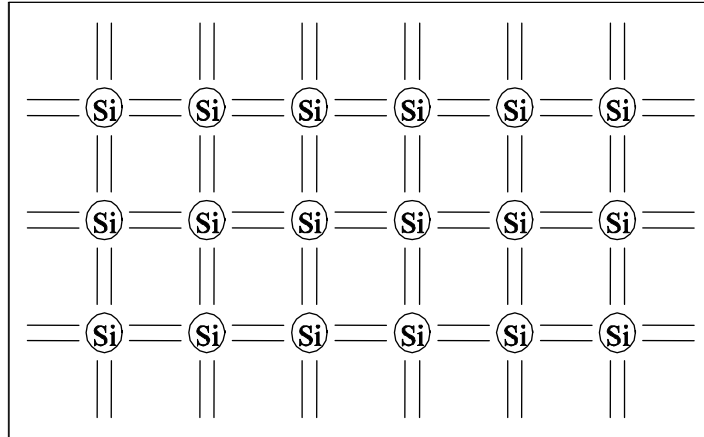


Figure 1. Two Dimensional Crystalline Lattice Structure.
This diagram represents a series of three dimensional tetrahedral structures [adapted from 4:27]. Semiconductors such as GaN have structures called wurtzite and zincblende.

inexplicable. The Kronig-Penney model isolates the wave-functions of a crystal by representing the atoms in a one-dimensional periodic potential [3:321].

Solving Schrödinger's equation using the Kronig-Penney model yields real and imaginary results for energy. Only real energy is permissible, so the imaginary results represent energies which are quantum mechanically forbidden. These forbidden energies define a region commonly referred to as the *energy gap*. Because these values are located in various bands, they are also referred to as the *band gap*. The permissible energies form regions referred to as the *valence band* and the *conduction band* [3:321-325], which are discussed below.

Another useful interpretation of the quantum mechanical picture is to consider the electronic energy levels of the hydrogenic model of the atom. In complete isolation, the energy levels are discrete quantum states. As atoms are brought together, the discrete wavefunctions of the electrons begin to overlap, and electron orbitals begin to broaden and merge and then split apart again. At the distances of a crystal (on the order of 1-2 Å

at room temperature), the electronic wavefunctions of nearest neighbor atoms merge (thus a covalent bond) and the orbital becomes an S-P hybrid. Pankove illustrates this theoretical approach for diamond in Figure 2 [5:2].

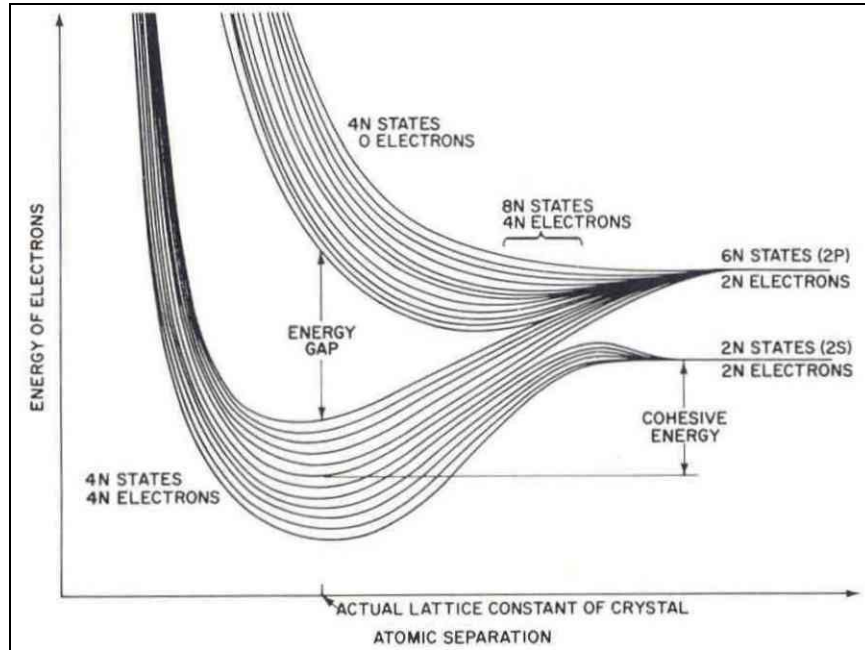


Figure 2. Merging of Electronic Orbitals.

Figure 2 illustrates an alternative approach for understanding the energy gap. Another important note about the crystalline structure of a semiconductor is that molecules are thermally oscillated about the lattice sites by quanta of energy referred to as phonons. Phonons most simply are a quantum mechanical vibration of the atoms. The vibration causes local changes in the energy structure which scatters free electrons as they encounter phonons while traveling through the lattice.

Dispersion Relation.

A dispersion relation is an expression which relates the frequency of a wave, ω , to the wavelength or wavenumber of that wave as it travels through a medium. As known from De Broglie, particles have certain wave-like properties; therefore the momentum, p ,

of a particle can be expressed by $\hbar k$ where \hbar is Plank's constant, h , divided by 2π and k is the spatial frequency or wavenumber [3:117]. Because energy, ε , is $\frac{p^2}{2m_0}$, where m_0 is the mass of the electron, free electrons have energy

$$\varepsilon = \hbar\omega = \frac{\hbar^2 k^2}{2m_0}. \quad (1)$$

From Equation 1, it is easily seen that the dispersion relationship of ω verses k equivalently expresses the energy-momentum relationship of a particle which behaves with wave-like properties.

The Kronig-Penney model of a periodic potential from atoms tightly bound together in a crystalline lattice structure can be combined with the free electron model to present a simplified model of a dispersion relationship for electrons in a semiconductor. An example of such a resultant dispersion relationship is shown in Figure 3. The

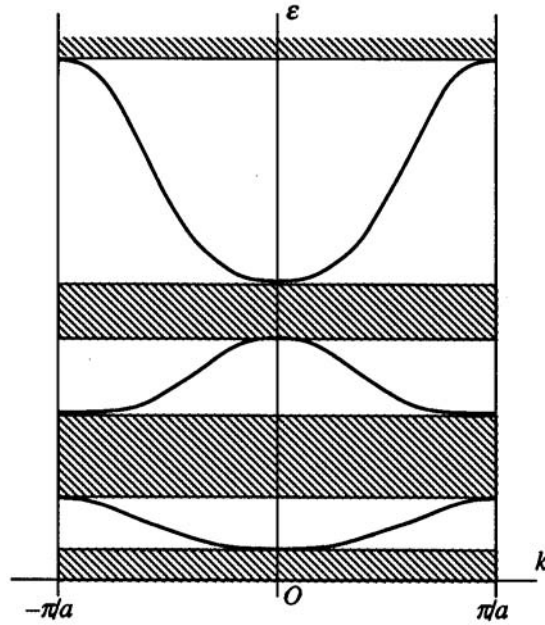


Figure 3. Dispersion Relation for Periodic Potential of Crystalline Lattice. Shading represents forbidden energy regions of the band gap [3:333].

dispersion relationship equivalence to the energy-momentum relationship also shows the energy band structure of electrons in the crystal.

Energy Band Structure.

According to Sze, the energy band structure of a material determines its properties of electrical conductivity. Metals have either overlapping valence and conduction bands (with no energy gap) or a conduction band which is partially full even at low temperatures. Metals are synonymous with conductors because they require very little energy for electrons to conduct. Insulators, on the other hand, have filled valence bands and many available states in the conduction band, but the energy gap is so great they require great amounts of energy before electrons become available for conduction [4:32].

Semiconductors are sometimes called poor insulators [3:363] because their band structure is similar to insulators but with a smaller band gap. At low temperatures, electrons are bound to the lattice site and are not available for conduction [4:27]. Unlike insulators, however, as temperature increases, thermal excitation of the lattice begins breaking the covalent bonds, and electrons begin to occupy the conduction band. This process is called *pair formation* because the electron leaves behind a positively charged “hole” where it used to occupy the covalent bond (hence, an electron-hole pair). These excited electrons are then available to move about the lattice in the presence of an electric field resulting in electrical conduction. Conversely, when an electron loses its excitation energy and recrosses the band gap, the electron-hole pair is eliminated in a process known as *carrier recombination*. Carrier recombination recreates the covalent bond which was broken by the electron excitation process. The mechanisms of carrier recombination will be explained in depth later.

It should be noted that the parabolic form of the free electron energy (Equation (1)) is only valid near $k = 0$, shown as the center of the diagram in Figure 3. It is common to assume electrons in motion through the lattice are free—even though they experience numerous atomic forces—but that the mass of the electron is changing. Because the mass does not really change, this varying value is called the *effective mass*, m^* . This assumption permits treatment of electrons and holes as if they are classical charged particles [4:31]. McKelvey expresses effective mass as

$$m^* = \frac{\hbar^2}{d^2 \epsilon / dk^2} . \quad (2)$$

[3:328]. This expression is constant near $k = 0$ where the parabolic approximation holds, but the equation holds even when the parabolic approximation fails.

It is notable that in a semiconductor there are typically three bands of holes and only one correspondent band of electrons. These three hole bands are usually doubly degenerate (six total), and because of the hybrid nature of the S-P orbital, the three bands of holes can be loosely corresponded to angular momentum P-orbitals in the hydrogen model. If an atom has a full P-orbital shell and an electron is excited, it will go to the next higher S-orbital. In a semiconductor, this is the conduction band.

Although the analogy is very loose, it is worth noting that even as hydrogenic energy values depend on angular momentum, the energy band structure of a semiconductor depends on angular momentum. The quantum mechanics of how angular momentum applies to the Kronig-Penney model are beyond the scope of this document; however, the implications are not. The top two valence bands are often referred to by

their effective masses: the heavy hole and light hole. The energy separation, Δ , between the split-off band and the other two bands at zone center is due to the quantum mechanical interaction of spin-orbit coupling [6]. All these energy band relationships are presented in a simplistic approximation about the point where $k = 0$ in Figure 4.

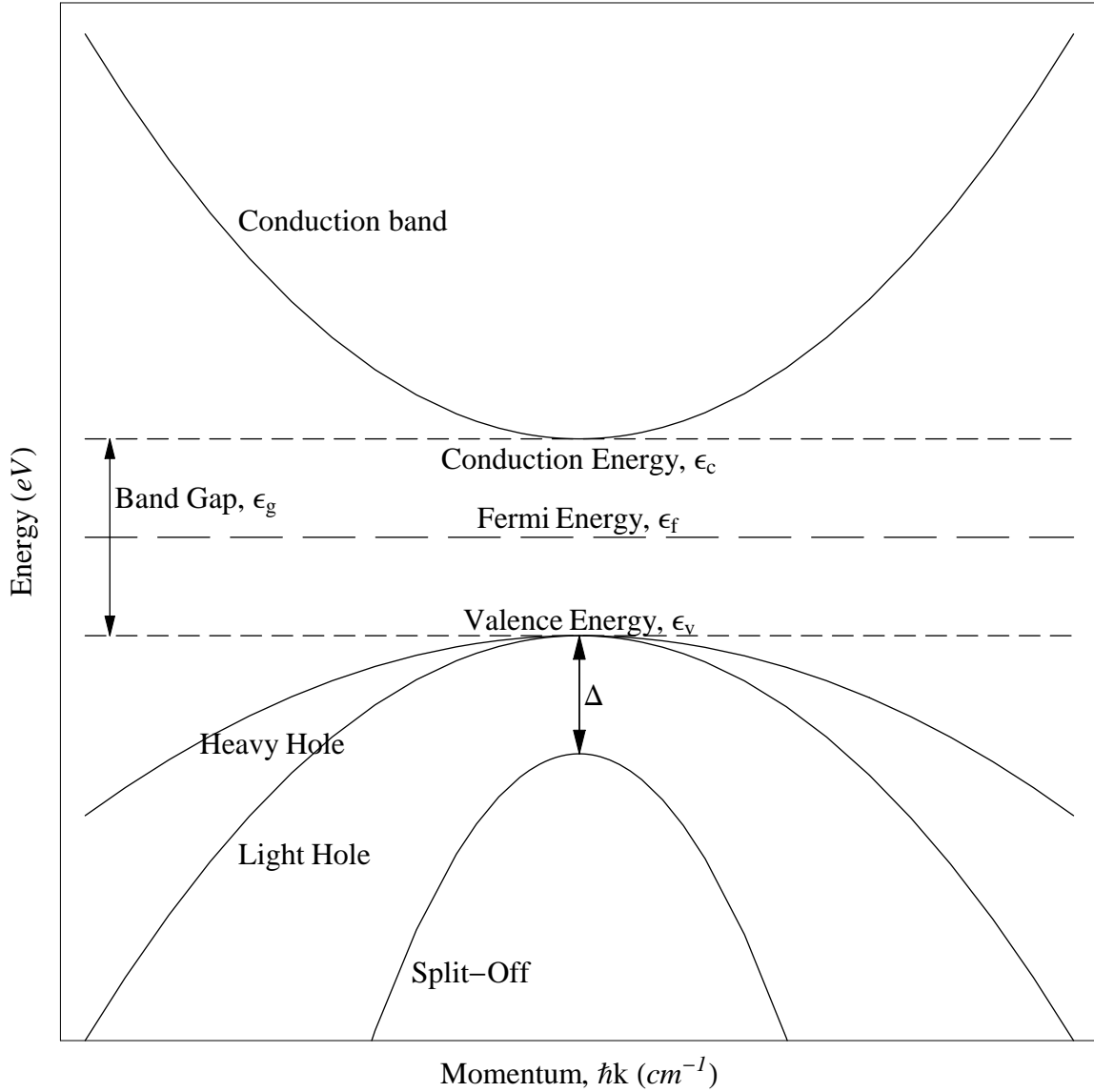


Figure 4. Notional Diagram of Energy as a Function of Momentum.

Figure 4 requires some explanation. Included are heavy hole (HH), light hole (LH) and split off (SO) bands. The energy relationships of charge carriers in

semiconductors determine which states are permitted by the quantum mechanics of a periodic structure, but the Pauli Exclusion Principle requires each energy state to be occupied by no more than one electron. Although energy states are discrete in nature, they are often treated as a continuum because a crystal with 10^{23} atoms has 10^{23} states in the conduction band. This is difficult to depict, but regardless of its treatment, an electron may only accept energy and momentum if it would be promoted to an unoccupied state.

Carrier Density

The unique character of semiconductors is determined by the behavior of the charge carriers (or just “carriers”) which are derived from a variety of factors. These include the density of states and Fermi functions combined with the energy band structure, temperature, and purity of the crystal. Figure 5 depicts these relationships graphically.

Carrier densities for electrons and holes, n_0 and p_0 , respectively, are determined in Equations 3 and 4:

$$n_0 = \int_{\epsilon_c}^{\infty} f_e(\epsilon, T) g_e(\epsilon) d\epsilon \quad (3)$$

$$p_0 = \int_{-\infty}^{\epsilon_v} f_h(\epsilon, T) g_h(\epsilon) d\epsilon \quad (4)$$

where $f(\epsilon)$ is the appropriate Fermi distribution (e for electrons and h for holes) and $g(\epsilon)$ is the appropriate quantum mechanical density of states [3:388]. These integrals represent the area under the top-most curves in Figure 5.

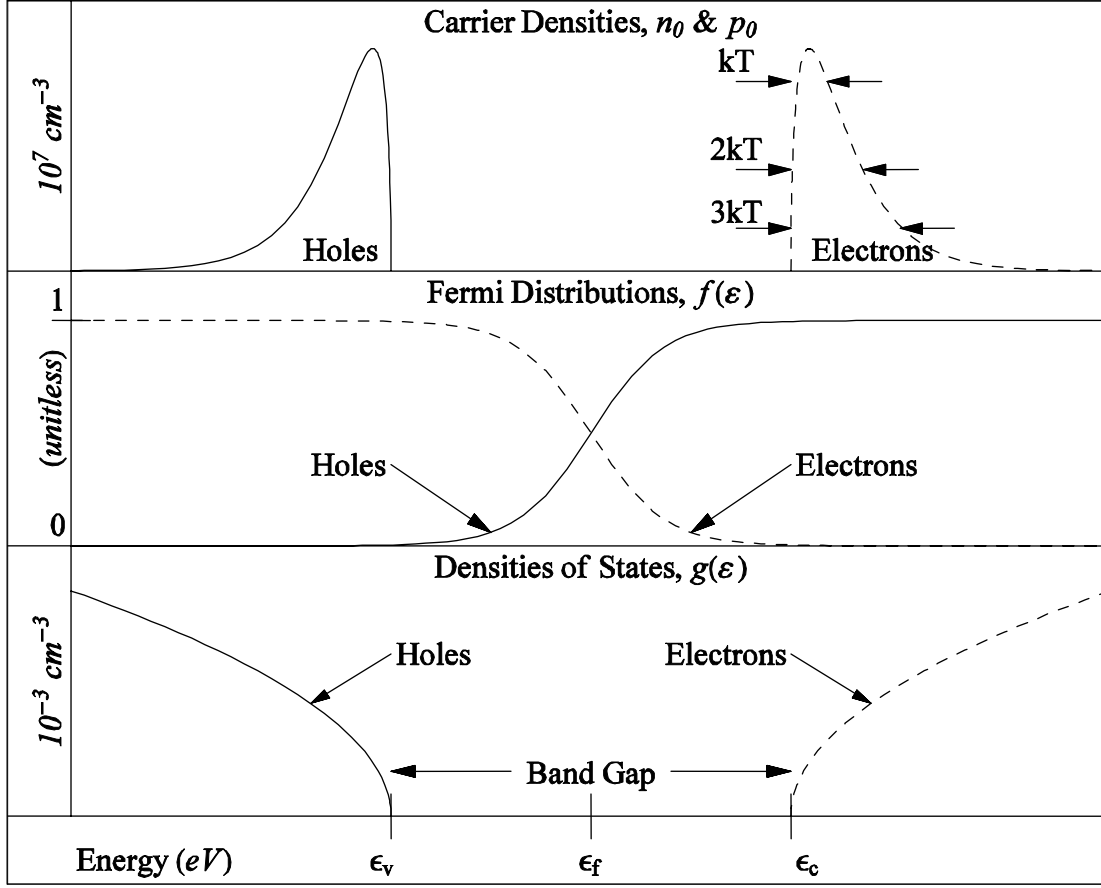


Figure 5. Theoretical Carrier Densities.

Dashed lines represent electrons and solid lines represent holes. The electron density illustrates the thickness of the electron distribution in terms of kT . The Fermi distribution is broadened with an exaggerated temperature (1500 K) and is assumed to be at band gap midpoint. For simplicity, the density of states are based on equal effective masses [adapted from 3:387].

The equilibrium density of states equation, $g(\epsilon)d\epsilon$, for electrons in the conduction band of a semiconductor is

$$g_e(\epsilon)d\epsilon = \frac{8\sqrt{2}\pi}{h^3} m_n^{*3/2} \sqrt{\epsilon - \epsilon_c} d\epsilon \quad (5)$$

where h is Plank's constant, m_n^* is the effective mass of the electron, ϵ is the energy and ϵ_c is the conduction band energy. The equilibrium density of states for holes in the

valence band is

$$g_h(\varepsilon)d\varepsilon = \frac{8\sqrt{2\pi}}{h^3} m_h^{*3/2} \sqrt{\varepsilon_v - \varepsilon} d\varepsilon \quad (6)$$

where m_h^* is the effective mass of the hole and ε_v is the conduction band energy [3:385-386]. Battacharya distinguishes the overall effective mass of the hole from its heavy hole (hh) and light hole (lh) contributors with this equation [3:65]

$$m_h^{*3/2} = m_{lh}^{*3/2} + m_{hh}^{*3/2}. \quad (7)$$

Electrons are distributed according to the Fermi-Dirac distribution function

$$f_e(\varepsilon, T) = \frac{1}{1 + e^{(\varepsilon - \varepsilon_f)/kT}} \quad (8)$$

where k is the Boltzman constant, ε_f is the Fermi energy and T is the temperature. Holes are the complement to electrons, so their distribution is $f_h(\varepsilon, T) = 1 - f_e(\varepsilon, T)$. The Fermi energy is the energy where the probability of occupation is $1/2$, and is typically located in the band gap for semiconductors. McKelvey derives the equation for the Fermi energy of pure (intrinsic) semiconductors as

$$\varepsilon_f = \frac{1}{2}(\varepsilon_c + \varepsilon_v) + \frac{3}{4}kT \cdot \ln\left(\frac{m_h^*}{m_e^*}\right) \quad (9)$$

where the band gap midpoint is $\frac{1}{2}(\varepsilon_c + \varepsilon_v)$ [3:390].

Effects of Impurities.

The ideal semiconductor has no impurities. Of course no real semiconductor is so pure, but a semiconductor whose impurity concentrations are small compared to the amount of thermally generated electrons and holes is called *intrinsic* [4:34]. By definition, the carrier density, n_i , in an intrinsic semiconductor is equal to n_0 which is equal to p_0 where

$$n_i^2 = n_0 p_0. \quad (10)$$

When impurities—whether naturally occurring or artificially inserted—influence the carrier concentration, the substance is said to be *extrinsic*, but Equation (10) holds true. Donors are any substance which has more electrons than would be present otherwise, and acceptors are any substance which likewise has fewer electrons (or more holes). These replacements are illustrated schematically in Figure 6 and Figure 7, which show a silicon crystal with an individual atom replaced with an acceptor and a donor, respectively.

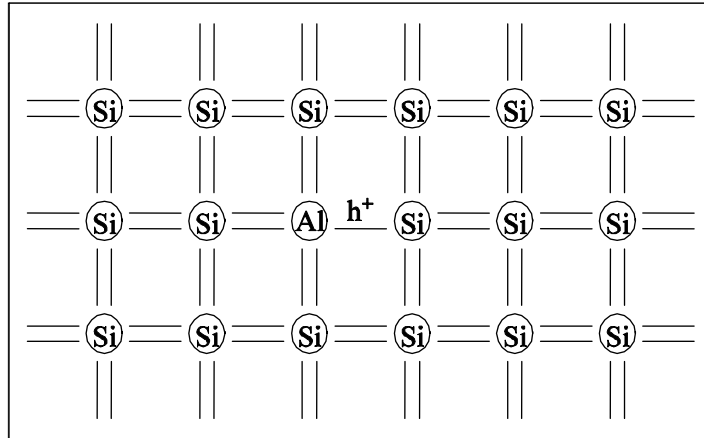


Figure 6. Silicon Lattice with an Acceptor.

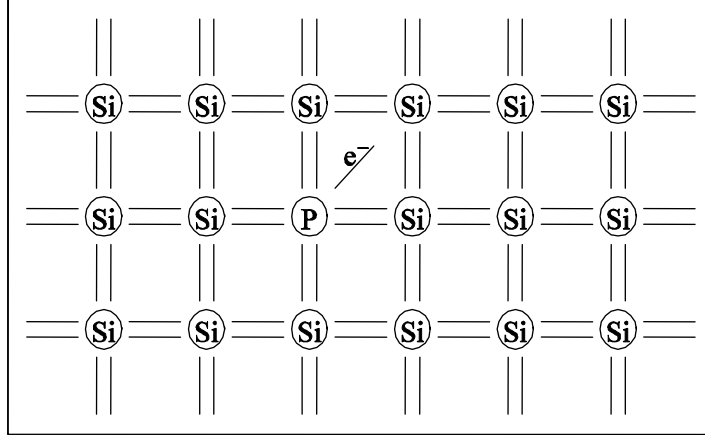


Figure 7. Silicon Lattice with a Donor.

Figure 6 and Figure 7 show single replacement atoms in a small area, but this occurs on a large scale throughout the crystal in large numbers—even in intrinsic materials—as shown in Figure 8. Typically with impurities, however, either the concentration of donors, N_D , or the concentration of acceptors, N_A , will dominate. When donors dominate, the material is called *n-type*, and when acceptors dominate, the material is called *p-type*. For *n-type* materials, McKelvey gives

$$n_0 = N_D \quad (11)$$

$$p_0 = \frac{n_i}{N_D}, \quad (12)$$

and for *p-type* materials,

$$p_0 = N_A \quad (13)$$

$$n_0 = \frac{n_i}{N_A} \quad (14)$$

[3:392]. These relationships are important for carrier recombination equations which

depend on the free carrier densities. Because impurities occur naturally, materials tend to be n -type or to p -type. If the difference in concentrations is balanced by adding donors to a p -type material or acceptors to an n -type material, intrinsic concentrations ($p_0 = n_0$) may be achieved. This material is referred to as a compensated material [7:88].

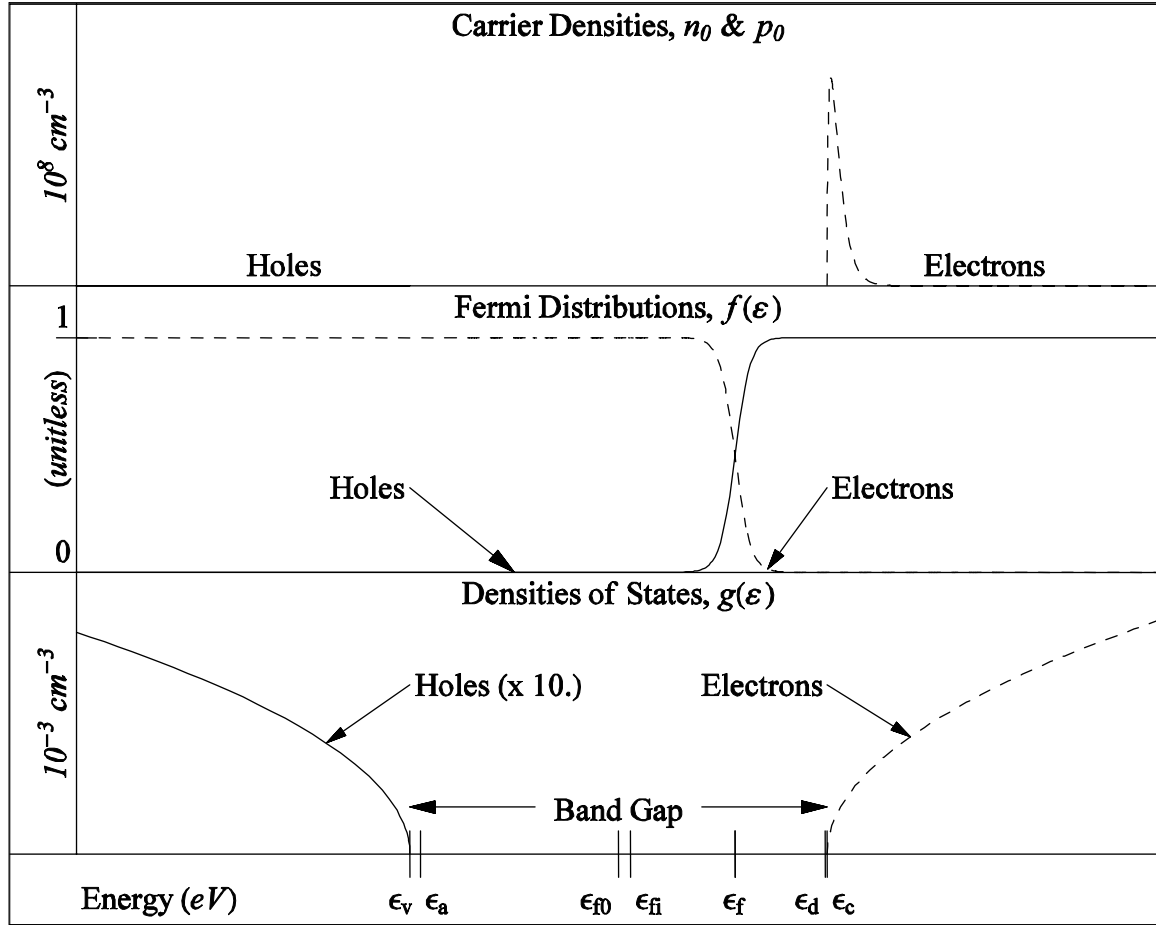


Figure 8. Increased Electron Density Due to the Presence of Donors. $N_D = 10^{14} \text{ cm}^{-3}$, $N_A = 10^{10} \text{ cm}^{-3}$ and $T = 300 \text{ K}$. The donor energy is more shallow than the acceptor showing that impurity concentration can dominate over impurity energy. Also shown are band gap midpoint, ϵ_{f0} , intrinsic Fermi energy, ϵ_{fi} , and Fermi energy, ϵ_f , from Equation (16) [adapted from Figure 5].

Intrinsic carrier concentration is, by definition, independent of impurities (for thermal equilibrium), as McKelvey shows

$$n_i = \sqrt{n_0 p_0} = 2 \left(\frac{2\pi \sqrt{m_e^* m_h^*} kT}{h^2} \right)^{3/2} e^{\varepsilon_g / 2kT} \quad (15)$$

[3:389], but Fermi energy changes with impurities as also shown by McKelvey

$$\varepsilon_f = \varepsilon_{fi} + kT \cdot \text{ArcSinh} \left(\frac{N_D - N_A}{2n_i} \right) \quad (16)$$

[3:391] where ε_{fi} is given as ε_f in Equation (9). Changing the Fermi energy changes the center of the Fermi distribution. Combining this change with Equation (3) quantifies the change in carriers depicted in Figure 8.

Effects of Temperature.

Figure 2 shows how the interatomic distance affects the band gap (distance increases to the right). It is a well-known phenomenon that increasing temperature of crystalline solids results in expansion (Figure 9), so inspection of Figure 2 shows that band gap energy typically decreases with increasing crystal temperature. The Varshni equation gives an empirical relationship for the band gap's temperature dependence:

$$\varepsilon_g(T) = \varepsilon_g(0) - \frac{AT^2}{T+B} \quad (17)$$

where A and B are experimentally determined parameters for a given substance [7:68]. For GaN, these parameters are $\varepsilon_g(0) = 3.47$ eV, $A = 7.7 \times 10^{-4}$ and $B = 600$ K [8]. Data confirming the lattice constants are shown in Figure 9 for the two axes of wurtzite (hexagonal) GaN [9], and empirical plots for the GaN bandgap are shown in Figure 10 [10:50].

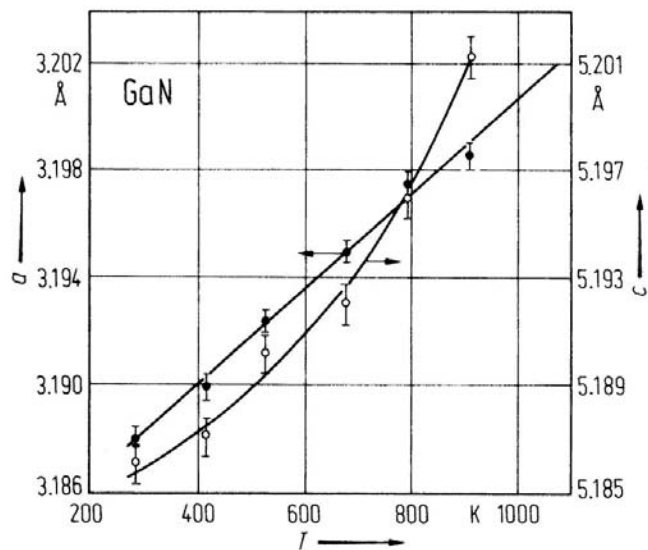


Figure 9. Lattice Constants as a Function of Temperature for Wurtzite (Hexagonal) GaN. The closed circles correspond to the left axis for the nearest neighbor distance, and the open symbols correspond to the right axis for the unequal crystal axis.

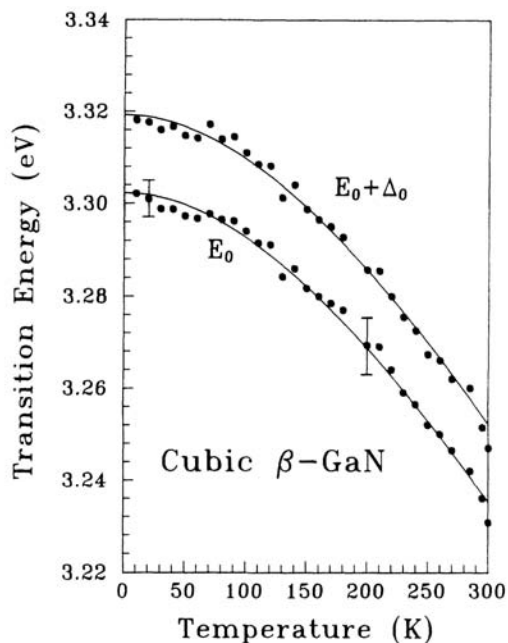


Figure 10. Band Gap as a Function of Temperature.

Although it has not yet been emphasized, the temperature dependence of the Fermi level has already been shown in Equation (9). For extrinsic materials, there is a

further dependence because the carrier densities shown in Equations (12) and (14) are also temperature dependent. This can be explained by the direct temperature dependence of the Fermi distribution (Equation (8)). In addition to these effects, carrier density is also temperature dependent due to electron ionization.

The mechanism for thermal excitation of electrons into the conduction band is phonon annihilation [3:375]. Phonons are quanta of acoustical energy which result from the oscillation of molecules in the crystal lattice [3:240]. At absolute zero, oscillation ceases, but as thermal energy increases, phonon concentration also increases. When a bound electron interacts with a phonon of energy greater than or equal to the band gap energy, the phonon is annihilated. This energy exchange annihilates the covalent bond, frees the electron and permits electron entry into the conduction band. Figure 5 depicts the energy dependence of electron density in the conduction band as a comparison to kT .

Carriers bound to impurity atoms but not covalently bound to atoms in the lattice behave differently than covalently bound electrons. The case of extra electrons on donors is simpler to understand, but holes interact similarly with acceptors. At low temperature, the electron is bound to the impurity atom. In similar fashion to carriers freed from the covalent bond by thermal excitation, the electron will eventually dissociate from the atom; however, donor ionization energy, ε_D , is much lower than the band gap energy. The relationship is determined by an equation similar to the hydrogen binding energy, ε_H , but modified by the effective mass of the carrier. Pankove relates the expression (in Gaussian units),

$$\varepsilon_D = \frac{m^* q^4}{2h^2 \varepsilon^2 n^2} = \frac{-13.6}{n^2} \left(\frac{m^*}{m_0} \right) eV \quad (18)$$

[5:9] where q is the fundamental charge, m_0 is the rest mass of an electron, ε is the permittivity of the semiconductor, and n is the principle quantum number. Pankove continues to explain that ε_D is usually on the order of 0.1 eV, so it is easy to see that ionization of impurities occurs at a much lower temperature than covalently bound electrons which are about 3.4 eV for GaN.

Effects of Temperature and Impurities.

Having shown the ionization energy of donors and its temperature dependence, it is useful to return briefly to comparisons with the hydrogenic model. As with the hybrid S-P orbitals, the analogy is useful, but very approximate. A major distinction in this case is the orbital radius. Whereas the Bohr radius, a_0 , of the hydrogen atom is \hbar^2/m_0q^2 [11:354], Pankove gives the radius of a hydrogen-like impurity in a semiconductor, a , as

$$a = \frac{\hbar^2 \varepsilon}{m^* q^2} = \frac{\varepsilon}{m^*/m_0} a_0 \quad (19)$$

where ε is the dielectric constant of the material [5:9]. Because the effective mass of an electron is much smaller than the rest mass of an electron (0.13 m_0 in GaN [8]), the orbital radius is much greater than the Bohr radius. Because this radius is greater than the interatomic spacing, there are many other atoms present within the donor electron's orbit. More accurately, the electron in Figure 7 and the hole in Figure 6 would not even fit on the diagrams.

The large orbital radius of donor electrons gives the electron a much larger domain of travel and hence greater opportunity to interact with other atoms in the lattice.

Even at low temperatures, this implies increased probability of encountering a displaced atom (a phonon) and hence a scattering that dissociates the electron from the impurity.

The combination of large orbital radius and the phenomenology of impurity ions dissociating due to phonon scattering makes it easy to see that any amount of temperature rise easily causes ionization of impurities throughout the crystal (Figure 11). This temperature dependence causes the carrier concentration at low temperatures to be highly dependent on the impurity concentration until all donors are ionized.

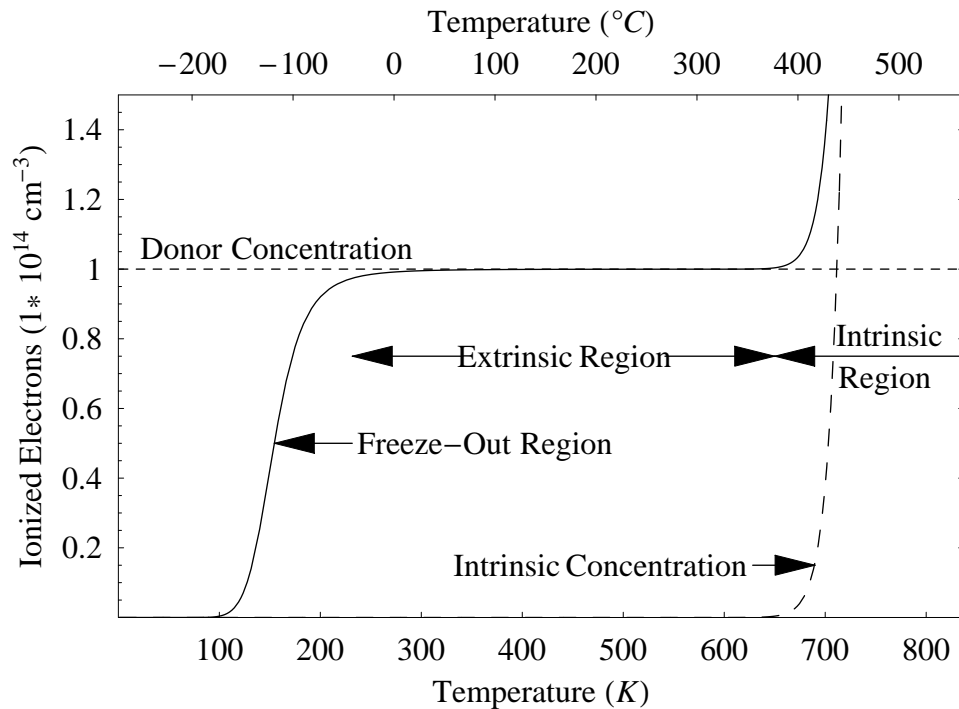


Figure 11. Carrier Concentration Dependence on Impurity Concentration and Temperature.

[Adapted from 4:42, based on properties of GaN].

The temperature below complete ionization is called the freeze-out region, and the temperature of complete ionization is called the extrinsic region due to the dependence on impurity concentration. As temperature increases past the extrinsic region, the lattice begins to vibrate severely enough that covalent bonds of the host atoms begin to

dissociate. This process is called thermal ionization, and the crystal enters the intrinsic region where carrier density is expressed as the sum of impurity concentration, N_d , and intrinsic carrier density, n_i (Equation (15)). Figure 11 illustrates these temperature dependent ionization regions.

Wolfe quantifies the low-temperature ionization of electrons as a ratio of neutral (unionized) donors to the total and the ratio of neutral acceptors to the total. These equations [12:129] can be solved for the number of ions. For electrons,

$$n_{ion} = \frac{N_d}{1 + g_d \text{Exp}\left[\frac{(\varepsilon_f - \varepsilon_d)}{kT}\right]} \quad (20)$$

and for holes,

$$p_{ion} = \frac{N_a}{1 + g_a \text{Exp}\left[\frac{(\varepsilon_a - \varepsilon_f)}{kT}\right]} \quad (21)$$

where N_d is the density of donors at energy, ε_d , from the conduction band, N_a is the density of acceptors at energy, ε_a , from the valence band and g is the multiplicity of conduction band minima (usually equal to one). As usual, ε_f is the Fermi energy, but it is not found in the usual manner.

In general, the Fermi energy may be determined with the following equation:

$$\frac{N_d}{1 + g_d \text{Exp}\left[\frac{(\varepsilon_f - \varepsilon_d)}{kT}\right]} - \frac{N_a}{1 + g_a \text{Exp}\left[\frac{(\varepsilon_a - \varepsilon_f)}{kT}\right]} =$$

$$N_c(T) \exp\left[\frac{(\varepsilon_f - \varepsilon_d)}{kT}\right] - N_v(T) \exp\left[\frac{(\varepsilon_v - \varepsilon_f)}{kT}\right] \quad (22)$$

[12:131]. Simplifying cases can be used to give the Fermi energy at certain temperatures.

First, for *n*-type materials, when the Fermi energy is within $4kT$ of the conduction band (low temperatures), Equation (22) yields a Fermi energy approximation of

$$\varepsilon_f = \varepsilon_d + kT \ln\left(\frac{N_d - N_a}{N_a}\right) \quad (23)$$

whereas at temperatures where the Fermi energy is below $4kT$ (high temperatures), the Fermi energy becomes

$$\varepsilon_f = \varepsilon_c - kT \ln\left(\frac{N_c}{N_d - N_a}\right) \quad (24).$$

Similarly for *p*-type materials, the low-temperature Fermi energy is approximated by

$$\varepsilon_f = \varepsilon_a - kT \ln\left(\frac{N_a - N_d}{N_d}\right) \quad (25)$$

and the high-temperature Fermi energy is approximated by

$$\varepsilon_f = \varepsilon_a + kT \ln\left(\frac{N_v}{N_a - N_d}\right) \quad (26)$$

[12:131]. Great care must be made for any approximation which may cross the transition between temperature regions.

Excitons

Free holes and free electrons experience Coulomb attraction and can bond together, forming a hydrogen-like pair where the electron orbits the hole. The energy of binding is an important value because it reduces the value of the free electron by the same amount, thus emitting a photon with lower frequency than a free electron does when the excitonic electron-hole pair is annihilated (recombine). Pankove gives the energy of a free exciton as

$$E_x = -\frac{m_r^* q^4}{2h^2 \epsilon^2} \frac{1}{n^2} \quad (27)$$

Where n is the quantum number of the excitonic state, and the reduced mass, m_r^* , is

$$\frac{1}{m_r^*} = \frac{1}{m_e^*} + \frac{1}{m_h^*} \quad (28)$$

[5:12]. Exciton energy levels are arbitrarily compared to the energy band gap with reference to the conduction band edge. This is to show that the energy yielded by an electron and hole formerly comprising an exciton is normally forbidden, as shown in Figure 12.

Discussion of excitons has so far been limited to free excitons which are an electron and hole bound together, but free to travel about the lattice. Excitons may encounter a local charge in the lattice (such as an ionized donor or an ionized acceptor) and become loosely bound to the charge. Although further detail will be omitted, the energy of binding will serve to further reduce the energy of the exciton [5:116]. The

importance of a particle's energy will become apparent in its effect on carrier recombination.

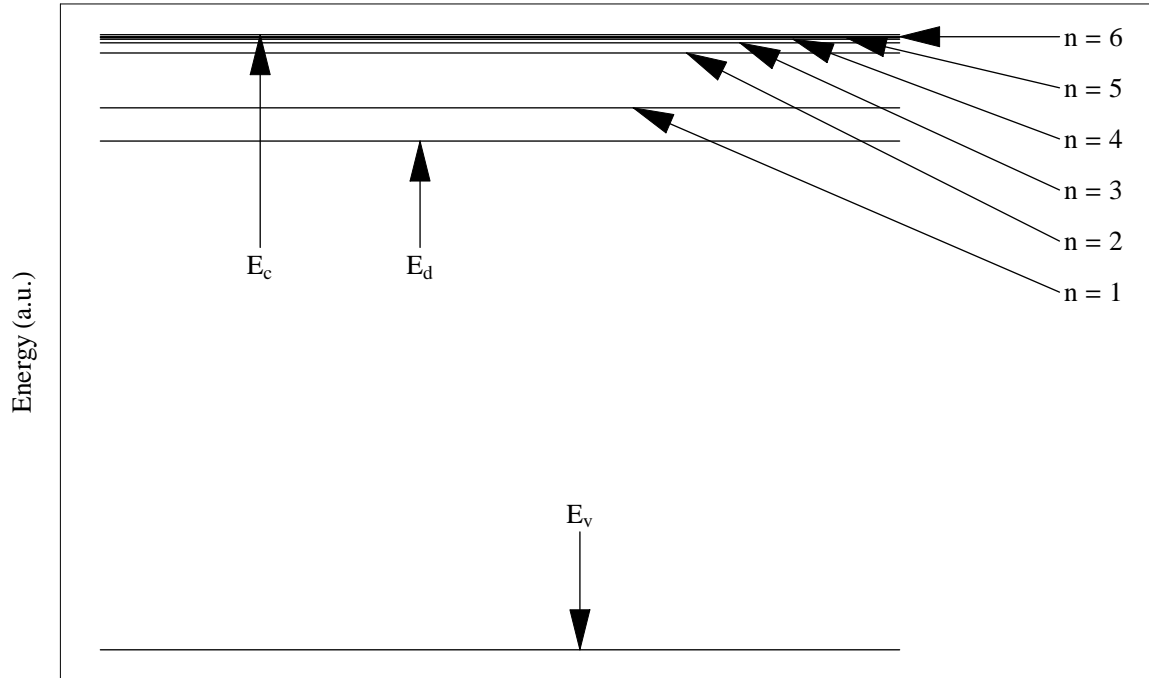


Figure 12. Energy Levels of Excitons.
The donor energy level is exaggerated for effect [adapted from 5:13].

Carrier Recombination

Carrier recombination is the non-equilibrium process which occurs when a free electron (not bound to the lattice) forfeits its free energy and combines with a hole to bond covalently. Both n_0 and p_0 are reduced by one. When a semiconductor is in thermal equilibrium, carrier recombination occurs at a rate equal to pair formation, thus carrier concentration is constant [7:114], and the amount of free carriers in equilibrium is determined by the conditions shown in Figure 11. In addition to the equilibrium carriers, n_0 and p_0 , *excess carriers*, Δn and Δp , may be generated by external forces applied to the semiconductor [12:236]. Total carrier concentration, n and p , are then given by

$$n = \Delta n + n_0 \quad (29)$$

$$p = \Delta p + \frac{n_i^2}{n_0} \quad (30)$$

[7:115]. Excess carriers recombine after the stimulus is removed. The carrier density reverts to the equilibrium condition determined by temperature and impurity concentration. Understanding the process of carrier recombination can provide great insight into the properties of the material.

Carrier recombination may occur radiatively where the energy of excitation is released via photon emission, or non-radiatively where the energy of excitation is transferred within the crystal. Generally, carrier recombination occurs both radiatively and non-radiatively, so the stimulation and subsequent radiative carrier recombination is called luminescence. Luminescence is further defined by the source of excitation: if caused by photon illumination, it is *photoluminescence*, if caused by electron bombardment it is *cathodoluminescence* and if caused by an electric field, it is *electroluminescence* [7:114]. Only photoluminescence was used in this research.

Radiative Recombination.

Radiative recombination occurs when an excited electron relaxes back into the valence band, both annihilating a hole and converting the energy difference between the two particles into an emitted photon. Figure 13 shows some common radiative transitions. Radiation can be considered a reverse process of photon absorption [5:107]. The energy of the particles depends on their positions in the dispersion relation (Figure 3 and Figure 5) also accounting for energy changes from impurities (Figure 8) and excitons (Figure 12).

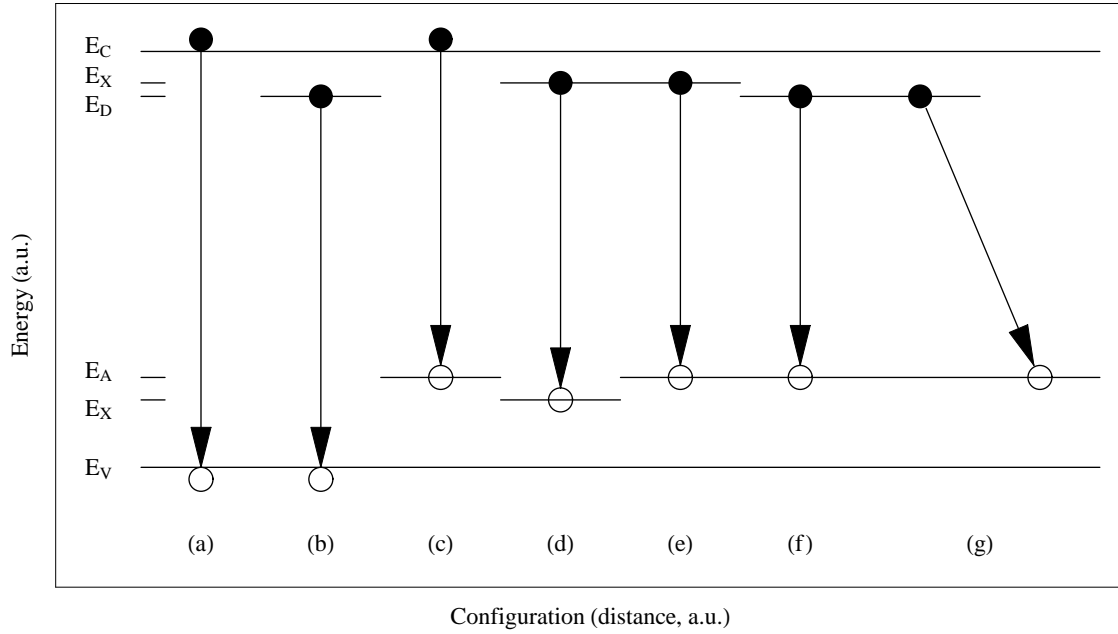


Figure 13. Types of Radiative Transitions.

Transitions are shown from highest energy to lowest energy. Solid circles are electrons and empty circles are holes. (a) Band to band, (b) neutral donor-to-valence band, (c) conduction band-to-neutral acceptor, (d) exciton bound to a neutral donor (e) donor-bound-exciton to neutral acceptor, (f) donor-acceptor pair (g) donor to acceptor at different lattice site [adapted from 13:18].

Radiative recombination is restricted by the population of electrons in an upper state available to recombine, as well as with the population of holes in a lower state available to receive those electrons. The radiative recombination rate, R , is simply a product of their densities with the probability, B , that such a transition will occur, or, from [5:111],

$$R = Bnp = Bn_i^2. \quad (31)$$

Non-radiative Recombination.

Non-radiative recombination is any mechanism of carrier recombination which does not emit a photon [5:160]. Because energy and momentum must be conserved, non-

radiative recombination must occur between a minimum of two particles. At the most general level, non-radiative carrier recombination is characterized by two-body interactions and three-body interactions (Auger processes). Two-body interactions may be interactions between either electrons or holes with defects in the material, phonons or interruptions in the periodic potential such as those induced by strain on the crystal or even the surface of the crystal. Three-body interactions are primarily amongst two electrons and a hole or two holes and an electron.

Measurement of these processes is difficult because by definition there is no light signal to indicate their presence. One can only measure emission efficiency, carrier lifetime and recombination kinetics [5:160]. As will be shown, the link between non-radiative recombination and these parameters exists in the mutual dependence between radiative and non-radiative recombination upon the time-dependent carrier density. Because light intensity is related to carrier density, a light signal still provides much information on non-radiative events.

Shockley-Read-Hall Processes.

As previously noted, perfect crystals are impossible to create, even under the most stringent conditions. Defects arise, such as an omitted atom, an interstitial atom located in a non-lattice site, or even replacements where an impurity atom occupies a lattice site “belonging” to another atom [7:103]. Shockley and Read, in their sentinel article, “Statistics of the Recombinations of Holes and Electrons,” first called these deep level defects “traps” because they trap electrons and holes which might otherwise have recombined fully across the band gap [14:835].

Besides providing electrons and holes, imperfections disrupt the periodic potential of the lattice. Solving the Schrödinger's equation becomes even more complex, but it is sufficient to recognize that the neat band gap pattern of Figure 4 is disrupted, and carrier transitions within the band gap become permissible at the location of the impurity. Consequently, these transitions are spatially dependent within the crystal. These energy levels may be deep in the band gap, and transitions between them and the conduction band are possible. These transitions may be radiative or non-radiative where the energy is transferred to a phonon. Even the radiative transitions deplete energy from the main region of energy transfer.

Carrier recombination dynamics inevitably involves discussion about the rates at which they occur. Without going into the development, the non-radiative recombination rate, R , of the Shockley-Read-Hall processes is given by [7:105]

$$R = s_r v_{th} N_T \frac{np - n_i^2}{n + p + 2n_i \cosh\left(\frac{\varepsilon_T - \varepsilon_f}{k_B T}\right)} \quad (32)$$

where s_r is the recombination center cross section, v_{th} is the thermal velocity of the carriers, N_T is the trap concentration, ε_T is the trap energy, and ε_f is the intrinsic Fermi Energy (Equation (9)). For a p -type material, where $p \cong p_0$, using Equation (10), it can be shown that Equation (32) simplifies to

$$R = A_{SRH} n \quad (33)$$

where the Shockley-Read-Hall constant, A_{SRH} is given by

$$A_{SRH} = \frac{1}{\tau_h} = s_r v_{th} N_T \quad (34)$$

thus defining the Shockley-Read-Hall recombination rate as being a function of the minority carrier density [7:105].

Auger Processes.

In their landmark paper on Auger processes, “Auger Effect in Semiconductors,” Beattie and Landsberg say the Auger process “may be thought of as a two-electron collision, the energy lost by one electron being taken up by another” [15:17]. This definition has been since expanded to include the hole created from the vacancy left by one of those electrons, thus defining Auger as a three-body process. Simply stated, a recombining electron collides with another electron which dissipates its new energy with phonon emission [5:161]. Several possible Auger processes are depicted in Figure 14.

Beattie and Landsberg conclude that the lifetime of excitation is given by the following equation

$$\tau \propto \left(\frac{E_g(T)}{kT} \right)^{\frac{3}{2}} \exp \left(\frac{1+2\mu}{1+\mu} \frac{E_g(T)}{kT} \right) \quad (35)$$

where μ is the ratio of effective masses for the electron and hole if $m_e < m_h$ or the reciprocal of that if $m_h < m_e$ [15:17]. The larger the band gap of a material, the larger the lifetime and hence the less impact it has on carrier recombination rates except at very high temperatures where there are higher carrier densities. Pankove extends this argument by saying that because this process is a carrier-carrier interaction, the greater the carrier concentration, the shorter the minority carrier lifetime. This can be expressed

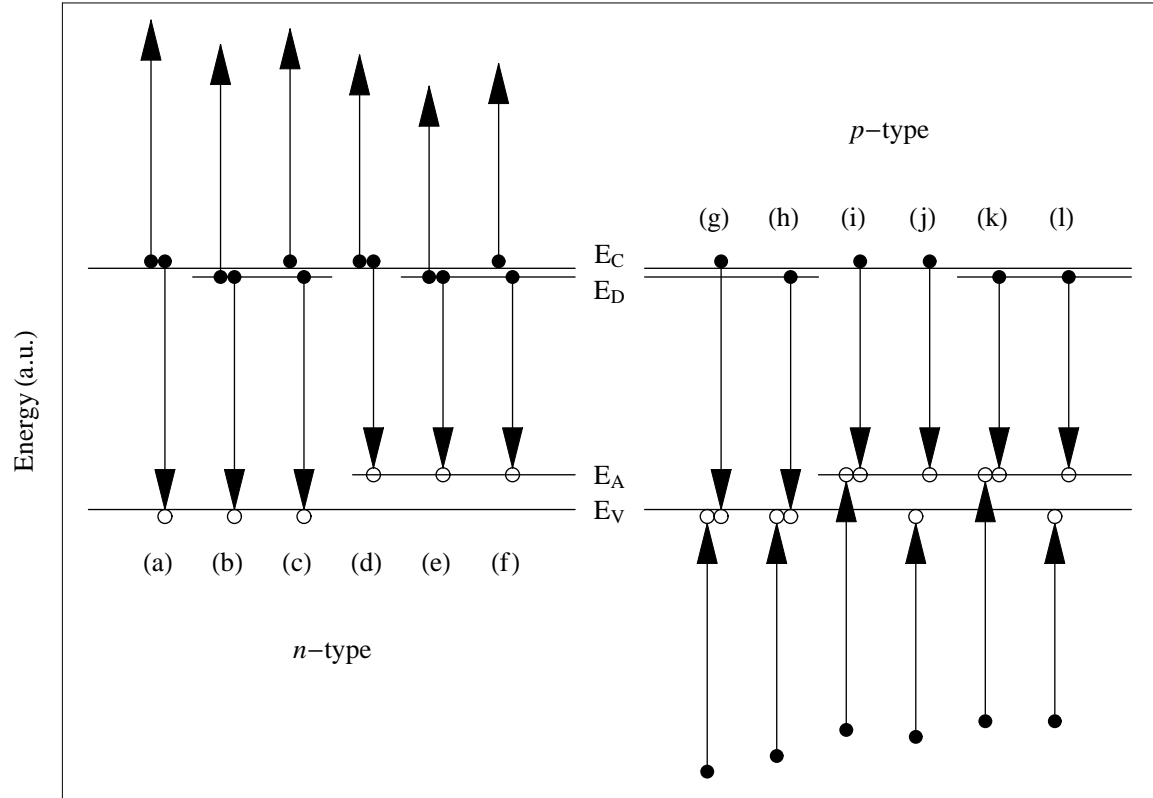


Figure 14. Auger Processes.
Processes (a)-(f) occur in n-type material and (g)-(l) occur in p-type material. [Adapted from 5:161].

for *n*-type and *p*-type materials as

$$\frac{1}{\tau} = C_0 np + Cn^2 \quad (36)$$

$$\frac{1}{\tau} = C_0 np + Cp^2 \quad (37)$$

where the C and C_0 are the Auger coefficients [5:162], which absorb the terms from Equation (35). For low values of Δn and Δp , the first term in Equations (36) and (37) is ignored and the rate of Auger Recombination becomes [7:148]

$$R = \frac{n}{\tau} = C_{Aug} n^3. \quad (38)$$

Carrier Recombination Rate

Accounting for all the recombination processes of the previous section, the total carrier recombination rate, R , may be expressed as the negative time rate of change in the electron density [12:239] and summarized by the following equation:

$$-\frac{dn}{dt} = A_{SRH}n + B_{Rad}n^2 + C_{Aug}n^3 \quad (39)$$

where n is the carrier density as a function of time, t . As was noted earlier (“Non-radiative Recombination.”), photoluminescent intensity can be used to find $n(t)$ and the link between experiment and theory is complete. Johnson outlines a clear procedure [16:3-4], followed closely here, which begins by finding the initial number of excess carriers.

The number of carriers generated by photoluminescence (Equation (29)) is equal to the number of photons exceeding the band gap which are absorbed by the semiconductor. For a laser pulse with energy, E_l , this value is $E_l/h\nu$. However, not all photons in the pulse will be absorbed. Losses due to surface reflection ($1-R_s$) and incomplete absorption (α) through the thickness, l , of the material $(1 - e^{-\alpha l})$ decrease this number. The total number of carriers, N , is then

$$N = \frac{E_l}{h\nu} (1 - R_s) (1 - e^{-\alpha l}). \quad (40)$$

Furthermore, unless the pulse completely floods the sample, only a certain volume of it will be illuminated. For a Gaussian beam of radius, w , this volume of illumination, V , is given—assuming no internal transport of excited carriers— by

$$V = \frac{\pi w^2}{\alpha} e^{-1}. \quad (41)$$

Combining Equations (40) and (41) gives the initial number of excess carriers $\Delta n(t_0)$ as

$$\Delta n(t_0) = \frac{E_l}{h\nu} \frac{\pi w^2}{\alpha} e^{-1} (1 - R_s) (1 - e^{-\alpha l}). \quad (42)$$

Johnson continues the argument by explaining how to map carrier density to measured luminescence [16:3-6]. He develops a link between luminescence measured to Equation (31) in the form

$$L = \eta B_{rad} n^2 \quad (43)$$

where η represents all the losses associated with receiving the photons to include system losses, extraction losses and the fraction of luminescence volume which is measured. He concludes that $n(L)$ is the inverse of the previous equation with background luminescence, L_{bg} , first subtracted from the measured value, as follows,

$$n(L) = \frac{1}{\eta B_{rad}} \sqrt{L - L_{bg}}. \quad (44)$$

Assuming constant background luminescence and letting $L'(t) = L(t) - L_{bg}$ and substituting the previous equation into Equation (39) gives the time rate of change in

measured luminescence, L' ,

$$-\frac{dL'}{dt} = k_1 L' + k_2 (L')^{3/2} + k_3 (L')^2 \quad (45)$$

where, for simplicity, $k_1 = 2A_{SRH}$, $k_2 = \sqrt{B_{rad}}/\eta$ and $k_3 = C_{Aug}/(\eta B_{rad})$. A curve for dL'/dt may now be fit and the Shockley-Read-Hall, radiative and Auger coefficients and lifetimes can be found directly from the fit parameters.

Fitting data to equations of this form requires that the many parameters discussed above be measured or known precisely (η includes many experimental parameters). Gorski reports that this relationship causes the greatest uncertainty in curve fitting the data [21:34]. Consequently, it is not uncommon for experimentalists to take a less rigorous approach to their data fit [17]. An example of such an equation is

$$L(t) = A \cdot e^{-t/\tau_1} + B \cdot e^{-t/\tau_2} \quad (46)$$

where τ_1 and τ_2 are the lifetimes of decay. Although it lacks the robust link to theory as shown in the above development, its simplicity begs its use.

Due to the exponential form of Equation (46), a logarithmic plot of the time-dependent data can be used to prepare the data for linear regression. Of course, one can not technically take the logarithm of the double exponential directly, but for limiting values of coefficients and lifetimes, two separate lines can be fit which do so (Figure 15). Linear regression is performed on data corresponding to low values of t and another is performed on data corresponding to high values of t . The τ values are the negative reciprocal of the slope, and the coefficients A and B are exponentials of the y-intercepts.

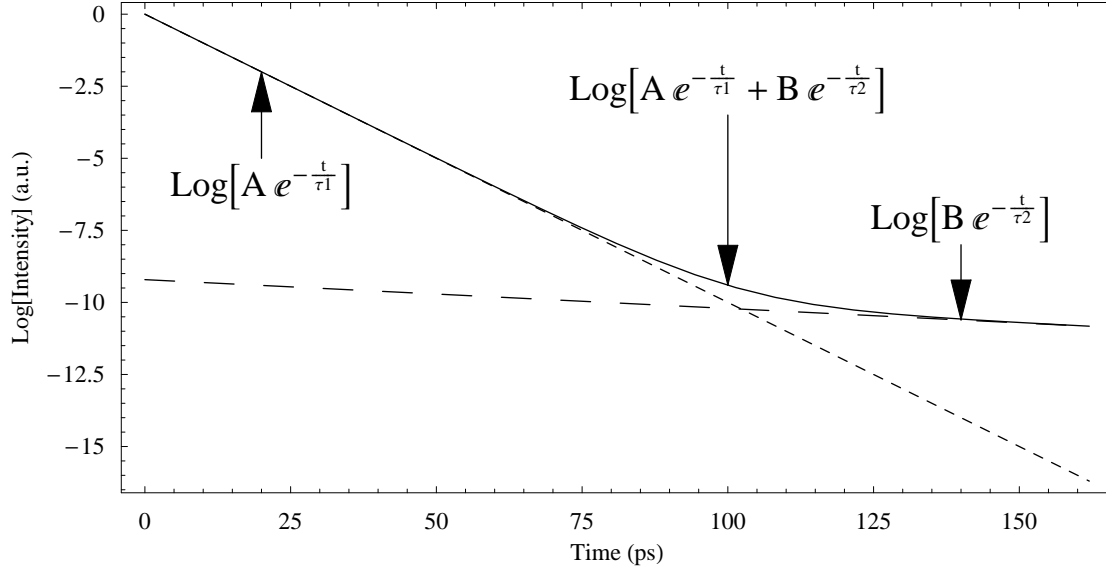


Figure 15. Logarithmic/Linear Plot of Double Exponential Equation.
For the plot, $A = 1$, $B = 10^{-4}$, $\tau_1 = 10\text{ps}$ and $\tau_2 = 100\text{ps}$.

Time Resolved Photoluminescence

Connecting the theory to experimental values still requires an experiment which can measure the luminescence of ultra-fast phenomena, both temporally and spectrally. Performing this measurement is accomplished with an experiment known as time resolved photoluminescence (TRPL). Gorski reports various methods of TRPL: upconversion, streak camera, photoconductive response and pump probe spectroscopy [18:5]. This TRPL experiment was performed using a streak camera; therefore, the other methods will not be discussed.

The source and detection system of a streak camera TRPL experiment make it unique. The source must be an ultra-short pulse laser, and the detector is usually a high resolution spectrometer with the streak camera used to analyze the dispersed signal. The following chapter discusses details of the experimental setup used to perform the TRPL experiment.

III. Experimental Setup

Time Resolved Photoluminescence Experiment

This is the first time-resolved photoluminescence (TRPL) experiment using the new streak camera at AFIT, building on the large legacy of AFIT TRPL experiments already performed on narrow band gap materials using upconversion [19, 20, 21, 22 and 23]. The experiment was performed in building 644, room L120 of the AFIT campus located in Area B of Wright Patterson Air Force Base in Dayton, Ohio.

The TRPL experiment consists of three sections: the laser system, the photoluminescence and the light measurement. The laser system has three major components: an argon ion pump laser, a titanium: sapphire ultra-short pulsed laser and a third harmonic generator. The photoluminescence occurs in a helium-cooled Dewar (helitran) which holds the sample. The light measurement section includes a spectrometer and an ultra-fast streak camera. The experimental layout is shown in Figure 16.

Included in this experiment is time-integrated photoluminescence (PL) data collection. The experimental setup is integrated into the TRPL experiment, but the light collection system is different. The spectrometer – operating as a monochromator – diverts light into a photomultiplier tube (PMT). The PL data are necessary to calibrate the spectrum of the streak camera and to verify the results.

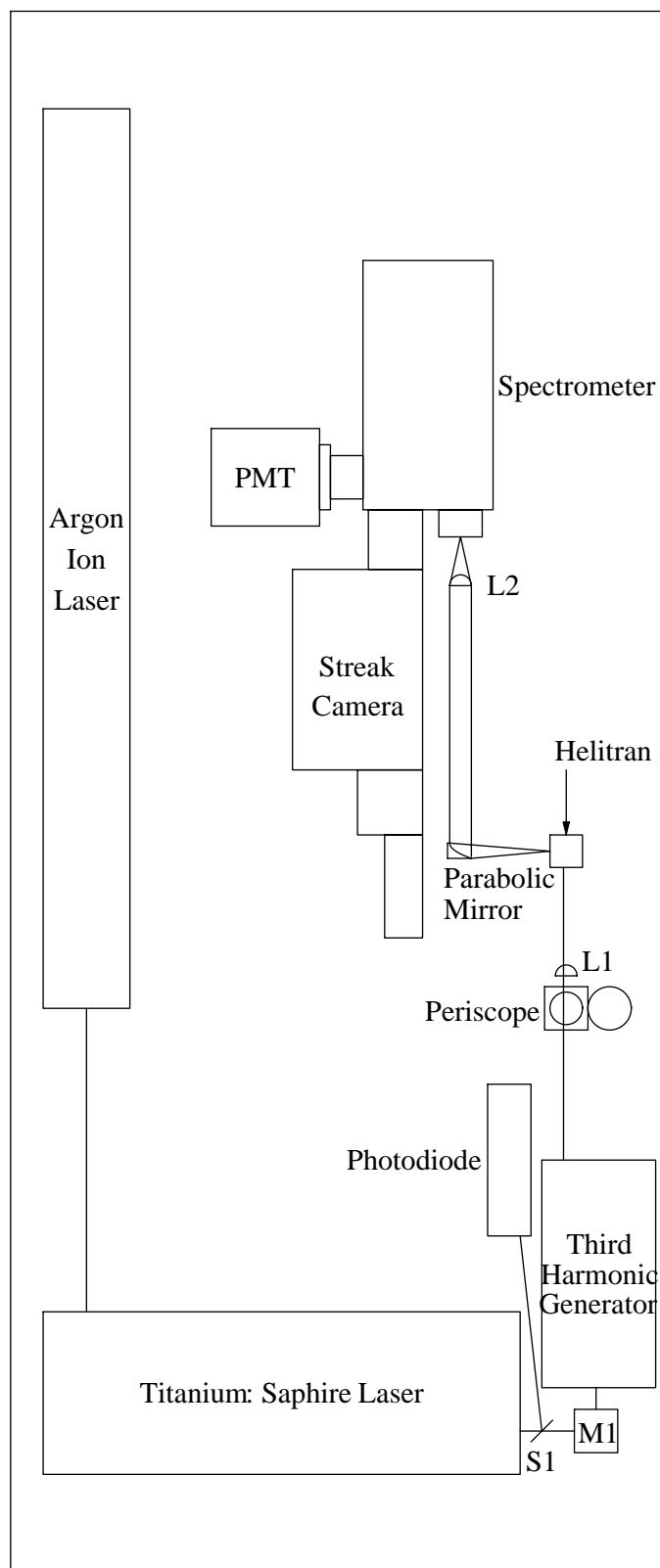


Figure 16. Experimental Setup.

Laser System.

The laser system has three major components: an argon ion pump laser, a titanium: sapphire ultra-short pulsed laser and a third harmonic generator. The laser system provides the light which stimulates the electrons in the sample. The argon ion laser is used to pump the titanium: sapphire laser. The titanium: sapphire laser provides ultra-short pulses. The third harmonic generator converts photons to those with an energy greater than the band gap of the material.

The argon ion pump laser is a Coherent Innova 400-F sealed mirror argon ion laser system (Figure 17) comprised of a power supply, a water cooling system, the Coherent Innova 400 laser head and a remote control module. This laser outputs a continuous beam tuned to the visible wavelengths in the argon spectrum and powered to 12W for the experiment.



Figure 17. Argon Ion Laser.

The argon laser is a pumping source for the titanium: sapphire laser. The titanium: sapphire laser is a Coherent Mira 900-F mode locked titanium: sapphire (Ti:Al₂O₃) ultra-short pulsed laser system comprised of a laser head (Figure 18) and a



Figure 18. Titanium: Sapphire Laser.

controller. The laser uses passive Kerr-mode locking to achieve an output pulse width measured by autocorrelation between 140 and 146 femtoseconds (fs). The wavelength was set to 810 nm for this experiment giving 790 mW of average power. The pulse repetition frequency (PRF) is 76 MHz giving a time between pulses of 13.16 ns.

The third harmonic generator (THG, Figure 19) provides additional wavelength tuning capability to the titanium: sapphire system. The THG is an Inrad M/N 5-050



Figure 19. Third Harmonic Generator.

As shown, primary beam enters on the left and sum-frequency generated light exits to the right through optional apertures.

Ultra-fast Harmonic Generation System. The system performs both second and third harmonic generation while maintaining minimum pulse broadening. Primary (810 nm), frequency-doubled (405 nm) and frequency-tripled (270 nm) beams may exit the device in various combinations. Second harmonic generation occurs in a lithium triborate (LBO) crystal, and third harmonic generation occurs in a beta barium borate (BBO) crystal [24]. Including losses from splitter S1 (Figure 16), average power from the THG was 7 mW unfiltered and 3 mW when the doubled and tripled wavelengths were filtered.

Photoluminescence.

The photoluminescence occurs in a helium-cooled Dewar called a helitran (Figure 20) which holds the sample in an evacuated chamber. Helium comes from the supply



Figure 20. Helitran.

Periscope and focusing lens are visible in the bottom right. The silver tube rising from the right comes from the vacuum pump. Samples are illuminated through the small circular window on the bottom right of the helitran, and photoluminescence is collected through the window on the bottom left.

Dewar via a vacuum-insulated transfer tube to the top of the helitran and drips onto a cold finger which suspends the sample in the vacuum chamber.

Light from the third harmonic generation system is raised by a periscope and focused (L1 in Figure 16) into one window of the helitran Dewar. Photoluminescence from the sample exits another window 90° from the entrance window. The laser beam terminates into a beam stop so only photoluminescence continues down the optical path.

Light Measurement System: Streak Camera.

Photoluminescence exiting the helitran window is collected by an off-axis parabolic mirror and collimated to a lens (L2) which focuses the light into the entrance slit of a spectrometer from an f-matched distance away. The spectrometer is a SPEX 500M which has a 1200 line/mm blazed grating at 5000 Å. The spectrometer has two exit slits: one into a photomultiplier tube (PMT) and the other into the ultra-fast streak camera. The PMT is used to perform time integrated PL measurements, and the streak camera is used to perform the TRPL. Because this study is the first experiment at AFIT involving the new streak camera, this special device is discussed in more detail below, giving attention to both the operation and the experimental setup.

Streak Camera Operation.

A streak camera is a device used “to measure ultra-fast light phenomena and [to] deliver intensity versus time versus position (or wavelength) information” [29]. The origins of streak cameras track to high speed rotating drum cameras which would streak light onto film. Modern streak cameras are electronic, and no other device offers better temporal resolution (on the order of 100’s of femtoseconds) [25].

Figure 21 depicts streak camera operation, which begins when light is incident on the instrument. The amount of light entering the instrument is controlled by a horizontal slit. Lenses then focus the incident light onto a photocathode which converts the photons

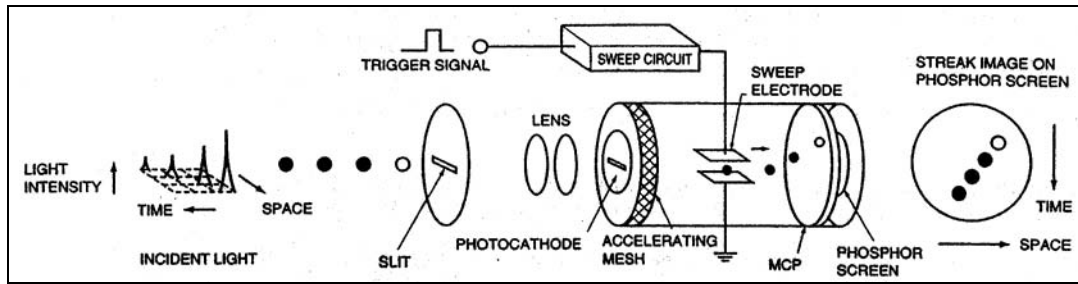


Figure 21. Streak Camera Operation.
[26:159].

into electrons and accelerates the photoelectrons through a chamber onto a micro channel plate (MCP). The MCP converts the photoelectrons into a signal which is imaged on a phosphor screen or read by a signal processor. Two sweep electrodes span the electron path in the chamber. These electrodes create a sinusoidally varying voltage across the traversing electrons so that electrons arriving at different times end up at different vertical positions on the image plane. The horizontal position of the electrons is undeviated through the instrument so measurement of the horizontal position may be calibrated to the photon wavelength if the light is spectrally dispersed prior to incidence on the streak camera.

An external trigger synchronizes the voltage sweep with the pulse repetition frequency (PRF) of the light source. A delay synchronizes the voltage sweep to coincide with the arrival of the light while overcoming differences in optical path length between the trigger and the arrival of light at the camera. Furthermore, varying the delay permits exploration of different time domains which is useful when investigating photoluminescent events which are temporally separated—as long as the temporal difference between the two is within the period of the selected time range.

The voltage sweep controls the temporal performance of the instrument as shown in Figure 22. Varying preset time ranges change the amplitude of the sweep voltage. Voltages outside the central region shown in the figure will deflect electrons away from the sensor (right axis) at the receiving end of the electron chamber. The amount of time that the sweep voltages are within the central region determines the period of time over which the sweep images. So the size of the sensor, the geometrical configuration of the chamber and the amplitude of the sweep voltages combine to determine the time range of the camera's image. The preset values for the camera used are shown in Table 1 [27].

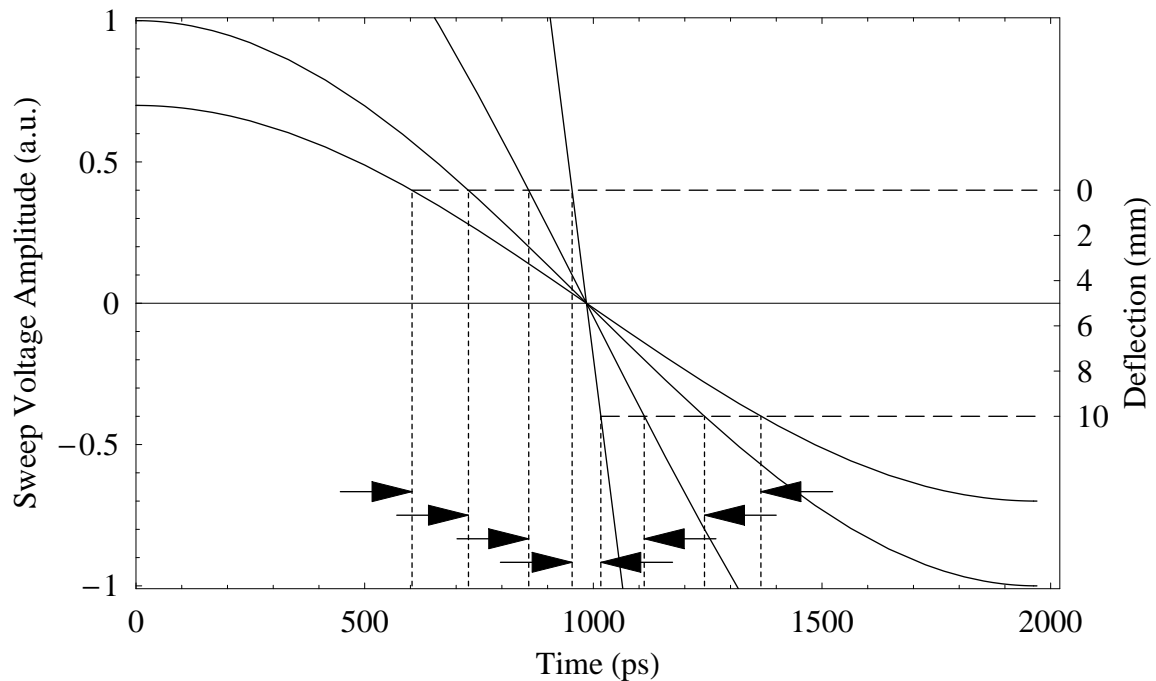


Figure 22. Relationship between Sweep Voltage and Streak Camera Time Range.

Table 1. Sweep Times for Time Range Control of the Streak Camera.

Time Range Setting	1	2	3	4	5	6
Time (ps)	45	101	203	492	1040	1970
Minimum Resolution (ps)	.758	2.42	20.8	27.2	31.3	42.3

Streak Camera Experimental Setup.

The streak camera used in this experiment is a Hamamatsu Model C6860 Synchroscan, shown in Figure 23. It was chosen with the S-20 head because of its spectral response characteristics as shown in Figure 24. The spectral response matches the wavelength of wide band gap semiconductors such as GaN which shows recombination phenomena between 300 and 500 nm. For simplicity and because the spectral width of the screen was found to be less than 4 nm in width (see section “Map of Pixels to Spectrum”), the optical response was assumed to be constant. Other relevant specifications include 45 ns trigger delay with jitter less than temporal resolution, 10 mm time axis, 9 mm spatial axis and 100 Hz maximum sweep repetition frequency. Complete specifications may be found on the Hamamatsu web page [28].



Figure 23. Hamamatsu Synchroscan FESCA C6860.
[29].

The streak camera trigger used light split from the beam at S1 (not to be confused with the “S-1” head shown in Figure 24) and incident on the photodiode as shown in Figure 16. Because an optical quality beam splitter was not available, a piece of

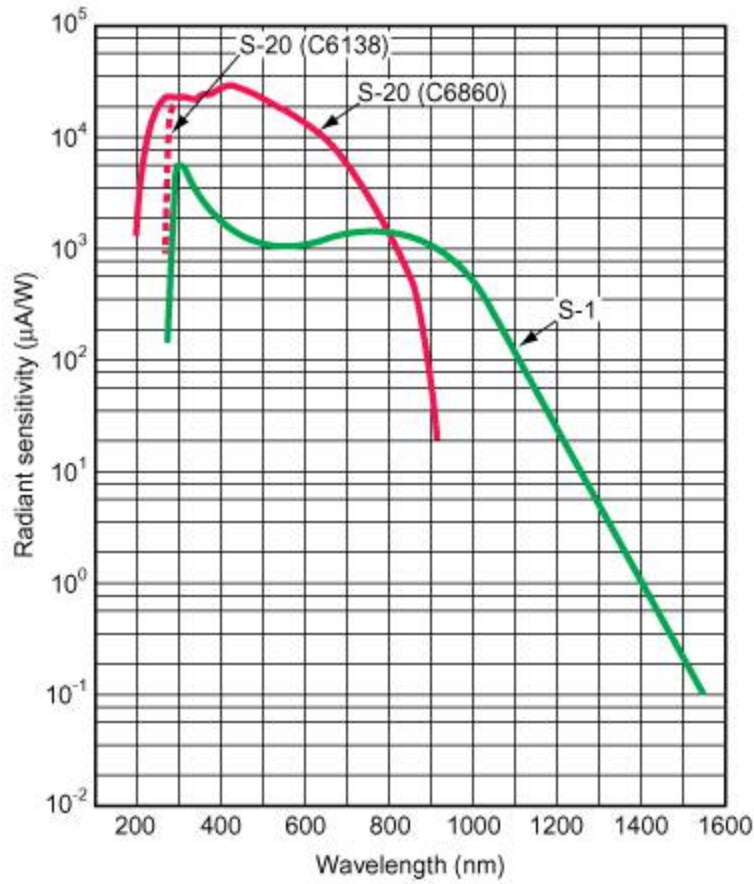


Figure 24. Spectral Response of the Hamamatsu C6860 Streak Camera. The S-20 C6860 sensor head (solid line) differs from the C6138 (dashed line) in the ultraviolet region [28].

household cling wrap was stretched across a circular frame to serve the function. The improvised device served the purpose well enough, but it split off so much light (35 mW) it saturated the detector (maximum 5 mW) when not attenuated.

Temporal Dispersion.

Temporal dispersion may be regarded as any mechanism which broadens the temporal profile of an event. Various sources of systematic temporal dispersion in an experiment include variations in the optical path length (OPL), spectral dispersion and streak camera sweep. Although it is not actually dispersive, streak camera slit widths can

effect the temporal measurement for the same reasons spectrometer slits effect the spectral measurement.

Variations in the OPL can usually be limited with high quality optics. Spectral dispersion is given by the following equation:

$$\Delta t = \frac{f}{F} \cdot \frac{k\lambda}{cd} \quad (47)$$

where f is the focal length of the spectrometer (0.5 m), F is an index of the lens used to focus light into the spectrometer, k is the order of diffraction, λ is the wavelength of diffraction, c is the speed of light and d is the groove interval (1200/mm) [30]. Finally, temporal dispersion in the streak camera is determined by the following equation:

$$\Delta t = \left(\Delta t_1^2 + \Delta t_2^2 + \Delta t_3^2 \right)^{1/2} \quad (48)$$

where Δt_1 is “electron transit time spread”, Δt_2 is “spatial resolution and deflection speed spreads”, Δt_3 is “deflection field spread” [31, 1-3].

New Equipment Setup

At the beginning of this research effort, the laboratory setup consisted of the operational argon ion laser, operational mode-locking, operational third harmonic generation and an operational streak camera that was mounted to a spectrometer but was not totally integrated into the system. Accomplishing Experimental Objective 1 (“Design, build and test an operational laboratory experiment which uses a streak camera to perform TRPL”) required new experimental setup and troubleshooting.

Equipment Installation and Integration.

Missing from the initial experimental configuration were the optics, a helium Dewar and a PMT. The helitran helium Dewar was found on hand and was suspended from the raised platform above the laser bench to avoid the clutter of assembling a make-shift scaffolding to support it from the laser bench. Location of the Dewar was inflexible once mounted, so the positions of all other components were determined by the Dewar or the laser (Figure 20). This proved to be problematic because any adjustment in the beam required complete realignment of the six degrees of freedom for an off-axis parabolic mirror.

The vertical position of the helitran was limited by its length and the necessity of being able to access the top for joining helium transfer assembly. The height difference between the helitran and the third harmonic generator required a periscope to raise the beam to the level of the sample. A pair of wedge prisms was chosen for this task. After the periscope, a lens was needed to focus the beam into the smallest possible spot size on the sample.

To collect the light emitted from the sample, an off-axis parabolic mirror was chosen because lenses have greater losses and maximum signal collection is optimal. The parabolic shape was necessary to collimate the light for its transfer to the spectrometer. Ideally, a second off-axis parabolic mirror would have been used to deliver the light to the spectrometer, but bench geometry could not afford such a configuration, and a lens f -matched to the spectrometer was used instead.

Additionally, a PMT was mounted onto the spectrometer resulting in a single platform containing the spectrometer, the streak camera, and the PMT. Once the optics

were positioned, the platform was raised to the height of the beam path. The spectrometer was focused and calibrated against a signal from mercury pen lamps. The streak camera was calibrated (for detailed procedure, see Appendix A) and the system was then ready to perform, but it was not yet ready for data collection due to several issues discovered during setup diagnostics.

Troubleshooting.

Obtaining reasonable temporal profiles from the streak camera was problematic. Upon third harmonic generation, the laser beam has an approximate pulse width of 250 fs. The minimal resolution of the streak camera is 758 fs [27]. Intuitively, one would expect the temporal profile of a laser pulse to appear as an image about the size of the camera's temporal resolution. Instead, a pulse width of 32 ps was initially observed. Furthermore, time integrated PL data showed distinct features. Some were captured on the streak camera, while others occurring at different wavelengths did not appear— either in “focus” mode (no sweep voltage from the camera) or “operate” mode (with sweep voltage). Data collection was discontinued until the source of the problem could be identified. Once these problems were identified and resolved within the constraints of resources, experimental data collection began.

IV. Experimental Data and Results

Overview

Because the primary goal of this research effort was to demonstrate a working system, much of the experimental data are system diagnostics, primarily spectrometer and streak camera operation. To demonstrate experimental effectiveness, data are also included from semiconductor photoluminescence, both time integrated and time resolved.

The major thrust of the system diagnostics was to determine how experimental controls varied the precision of the results. The experiment is a very complex setup, and not all interactions could be thoroughly understood in the brief time available. The most notable effects were studied, but further research may be necessary to quantify interactions between controls and results – especially after modifications to the setup.

Spectrometer Data

In this effort, the spectrometer was calibrated and joined to the streak camera. The close dependence of the streak camera on the spectrometer requires that its performance be well characterized. This was done in terms of spectral accuracy and spectral precision with the latter being expressed in terms of the trade-offs between resolution and signal strength.

Spectral Accuracy.

Mercury vapor lamps were used to determine the accuracy of the spectrometer because their wavelength is well known, the spectral lines of mercury span the wavelength region of interest for the materials under investigation, the spectral features

are sharp and distinct, and lamps were available for use. Lamps were illuminated into the spectrometer, and the position was varied to collect intensity points on the PMT. Peak positions were located and compared to known values [35]. The error in these values is presented graphically in Figure 25. Although the results reveal a potential systematic error, effort was not made to determine the source because of its trivial size.

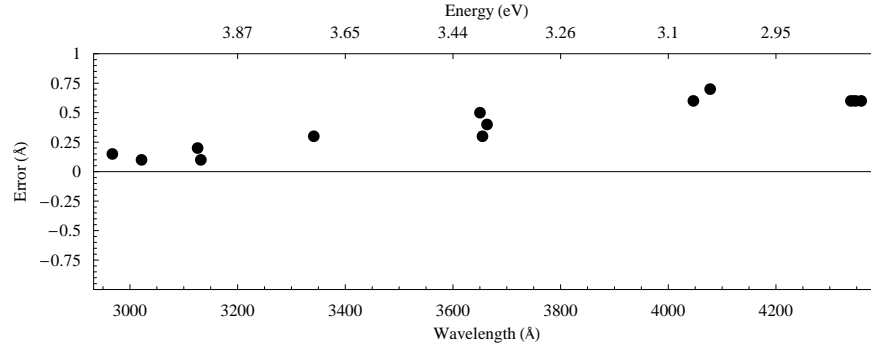


Figure 25. Wavelength Error in Spectrometer.

Spectral Resolution Versus Signal Strength.

Spectroscopy suffers from the well-known trade-offs between resolution and signal strength. A vertical entrance slit determines how much light is available for dispersion. Opening the slit width, w , strengthens the signal but reduces its resolution, $\Delta\lambda$. This is quantified by the following equation

$$\Delta\lambda = \frac{aw}{fm} \quad (49)$$

where a is the groove spacing, f , is the focal length of the spectrometer and m is the mode number of the reflection [32]. PL spectra collected for analysis with Equation (49) are shown in Figure 26. Representing the data from Figure 26 as a plot of spectral resolution versus slit width shows how well the data fit Equation (49). This is shown in Figure 27.

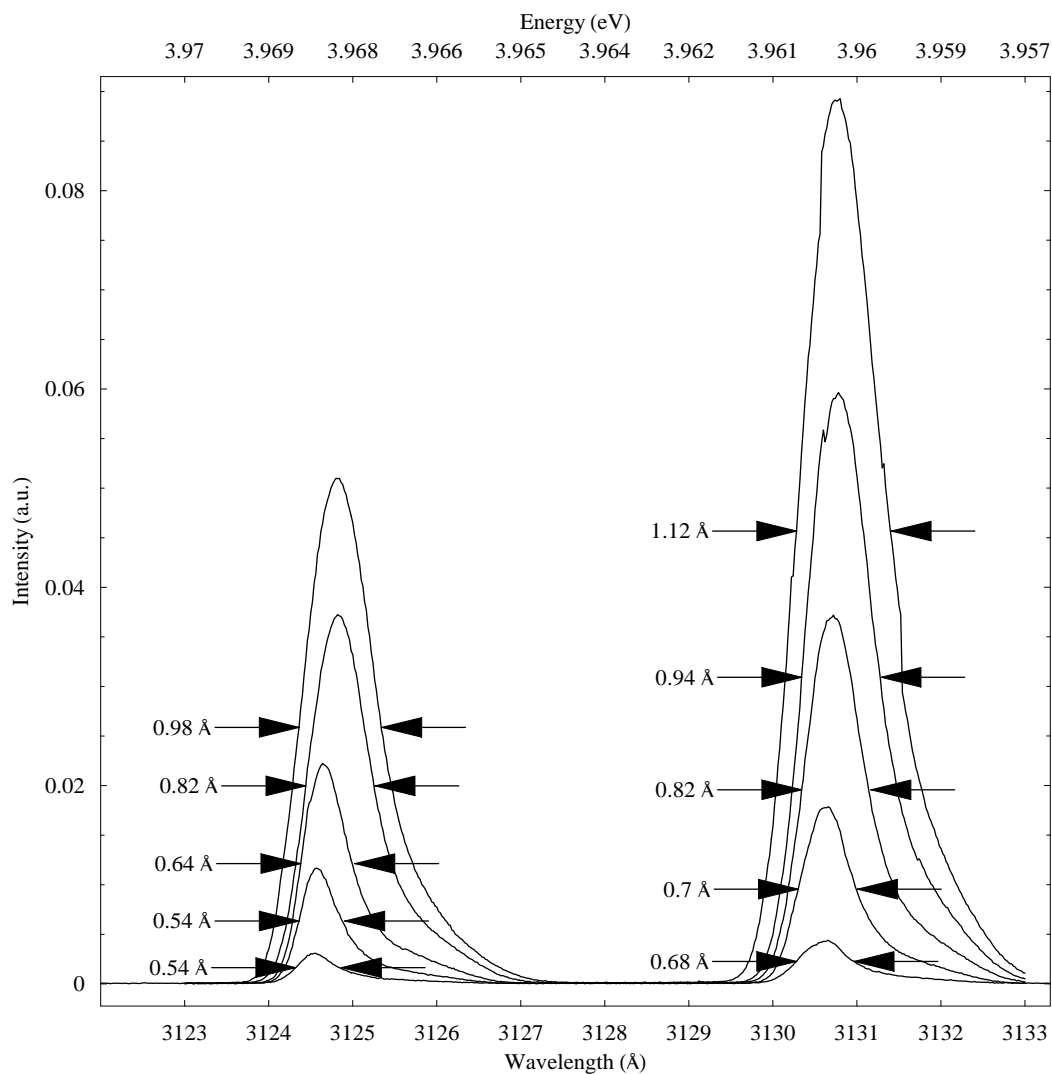


Figure 26. Mercury Doublet Resolved on Photomultiplier Tube (PMT). Spectrometer and PMT slit widths for peaks, tallest to shortest, are 60 μm , 50 μm , 40 μm , 30 μm and 20 μm .

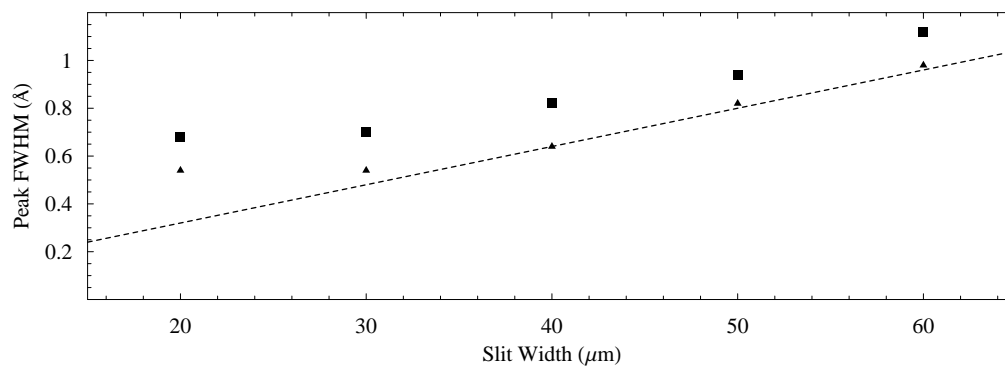


Figure 27. Spectrometer Spectral Resolution versus Slit Widths.

Streak Camera Data

Effective use of the new streak camera requires its performance to be characterized. Some of the performance characteristics were documented in the manufacturer's test report [27]. Most of this research effort focused on characterizing the temporal and spectral performance of the camera as set up in the AFIT laboratory.

Spectral Data.

As was shown in Figure 21 and supporting text, a streak camera may be used as a spectrograph if light entering it is spectrally dispersed. The SPEX spectrometer performed this task, but the camera only measures a physical distance (horizontal) which is measured in pixels. To determine what portion of the spectrum the streak camera is viewing, the spectral image must be calibrated to the spectrometer. This calibration permits spectral data to be mapped from pixels to spectrum.

Map of Pixels to Spectrum.

To calibrate the streak camera spectrum, spectral analysis of a mercury vapor lamp was performed using the PMT over a span of wavelengths which include a doublet (Figure 28). Light output from the spectrometer was changed to the streak camera and the spectral image was collected again (Figure 29). Temporal data was not needed for this task. Because the two data sets captured the same spectrum, the pixels on the streak camera could be converted to wavelength and energy (Figure 30). For detailed calibration procedure, see Appendix A.

The PMT collects a series of monochromatic data points, while the streak camera collects a fixed spectrum which depends on spectrometer position and streak camera focusing. Consequently, spectrometer position must be recorded in the laboratory

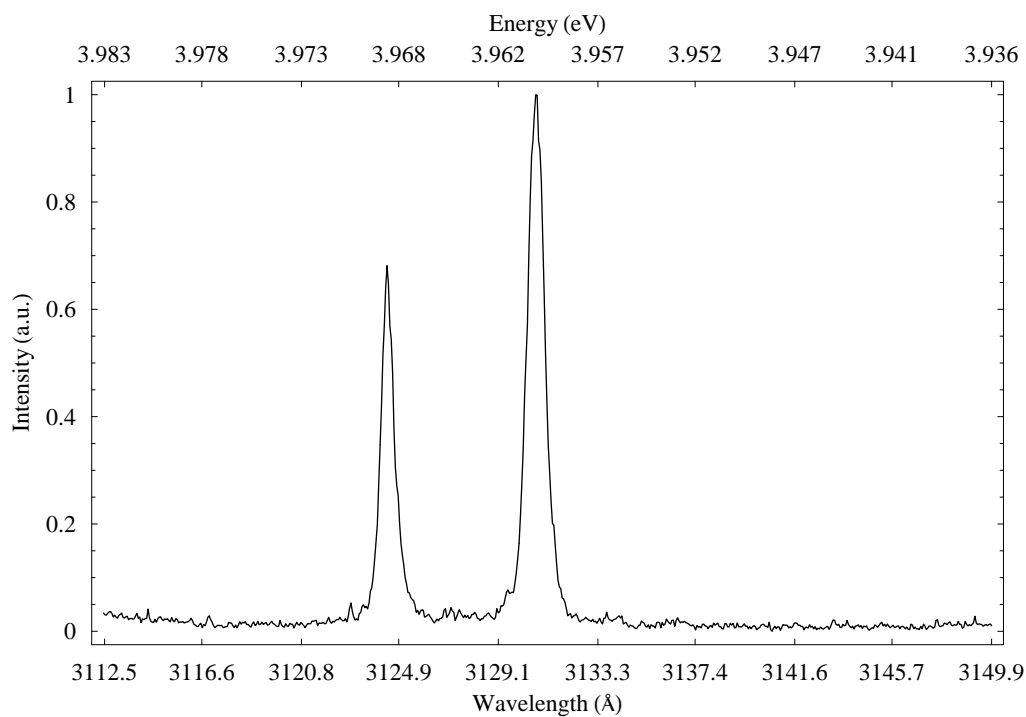


Figure 28. Spectrum from Mercury Doublet as Recorded on PMT.

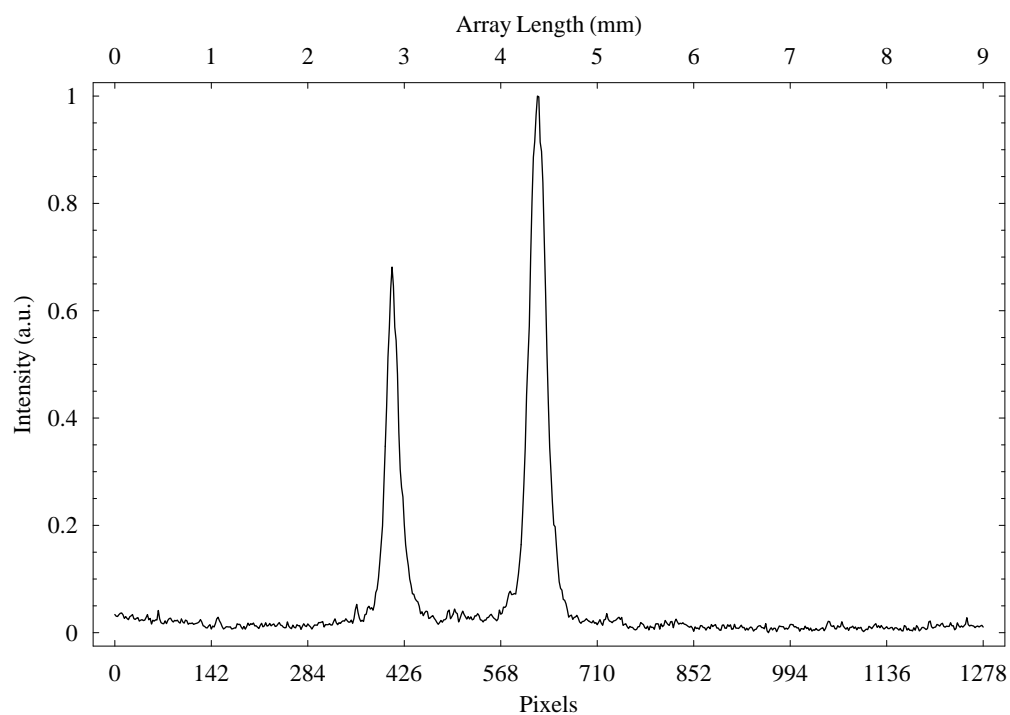


Figure 29. Spectrum from Mercury Doublet as Recorded on Streak Camera.

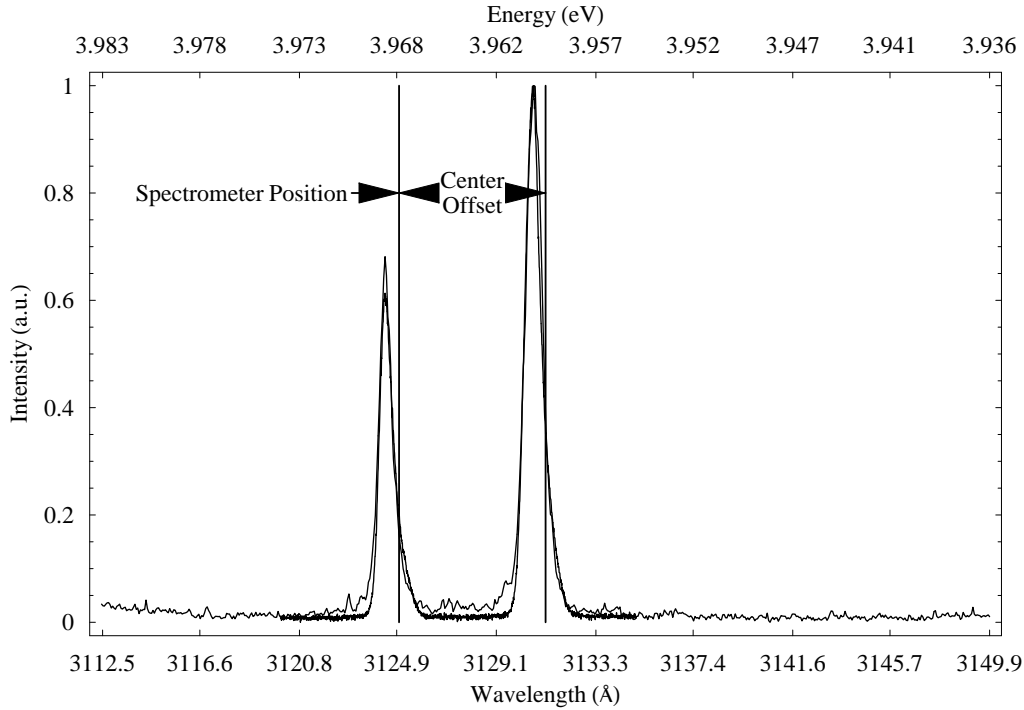


Figure 30. Mercury Doublet Image from Streak Camera Mapped to Spectrum. The line shows where the spectrometer was positioned spectrally when capturing the streak camera image.

notebook for any spectral data, and the calibration procedure must be repeated any time the camera is focused. Also, there is no guarantee that the spectrometer position is centered on the streak camera spectrum as shown in Figure 30. Ideally, the streak camera is in perfect vertical alignment with the spectrometer. Any change in this position requires the map of pixels to spectrum to be repeated.

Data were collected at several different spectral positions where mercury doublets are available. Calculations from these data yielded several parameters: scaling ratios of Angstroms to pixels, the spectral widths of the streak camera and the spectrometer offsets from the center of the streak camera screen, as recorded in Table 2. The scaling ratio can be used to convert streak camera spectral data from pixels into Angstroms when the spectrometer position is added to them. The spectral widths represent how wide of a

spectrum is captured on the streak camera. (These values are depicted in Figure 40.) The center offset is useful to keep in mind when trying to locate a spectral feature because the spectrometer position will be displaced from the center of the streak camera spectrum by this amount. These values are dependent on the focusing setting of the streak camera and must be recalculated if the streak camera focus is changed.

Table 2. Map of Streak Camera to Spectrum.

<i>Spectrometer Position</i>	<i>Scaling Ratio</i>	<i>Spectral Widths</i>	<i>Center Offset</i>
3125 Å	0.0290 Å/pixel	37.2 Å	6.1 Å
3650 Å	0.0285 Å/pixel	36.4 Å	4.0 Å
5774 Å	0.0284 Å/pixel	36.4 Å	2.9 Å
Average	0.0287 Å/pixel	36.6 Å	4.3 Å

Spectral Resolution Versus Signal Strength.

As with the spectrometer, the streak camera suffers from the spectroscopy trade-off between resolution of an image and the strength of the signal. Figure 31 and Figure 32 are comparable to Figure 27 and Figure 26 respectively. Figure 32 shows spectral profiles captured on the streak camera with varying slit widths on the spectrometer input slit. Streak camera data are summarized in Figure 31. It is important to recall that when

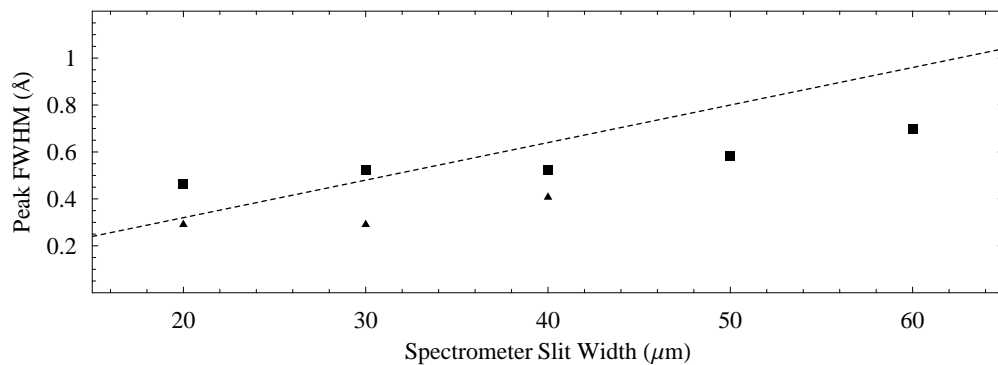


Figure 31. Streak Camera Spectral Resolution Versus Spectrometer Slit Width.

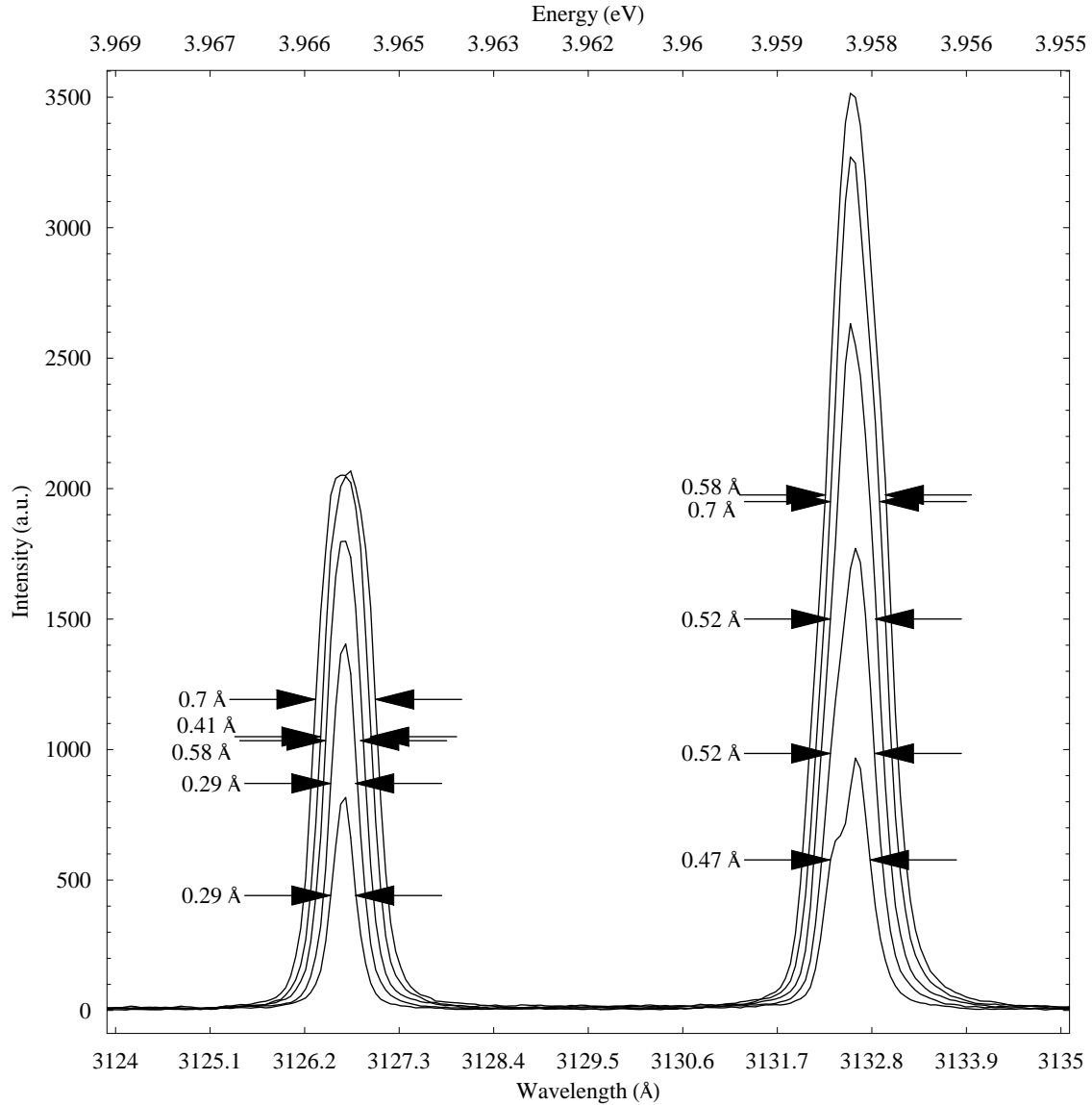


Figure 32. Mercury Doublet Spectrum Resolved on Streak Camera.
Spectrometer slit widths for peaks, tallest to shortest, are 60 μm , 50 μm , 40 μm , 30 μm and 20 μm .

the spectrometer outputs its light to the streak camera, there is no control over the horizontal width of the exit. The individual pixels in the photocathode of the streak camera serve as effective horizontal slit widths.

Temporal Data.

While the spectral data from the streak camera are useful to compare to the PMT spectra, temporal data acquisition is what makes the streak camera a unique instrument. Capitalizing on the precision of a streak camera to measure ultra-fast phenomena requires great precision in introducing light to the instrument. To obtain the most precise and accurate results, the light must not be vertically dispersed beyond the limits of instrument resolution. Temporal dispersion was diagnosed within the constraints of available tools, and effects on temporal resolution were studied as a function of various experimental controls including time range of the sweep voltage, streak camera slit width and spectrometer slit width.

Achieving temporal resolution within the limits of the instrument proved to be a difficult task. The effort was successful when vibrations were eliminated and when the streak camera was perfectly aligned with the streak camera. When vibrations were present or the alignment was off, temporal resolution was far from the instrument limit.

Temporal Dispersion from Vibration.

There are many sources of vibration in the experimental setup. These include a lab bench resting directly on the floor supports, two of which rest on a trench lid (not the solid floor itself); cooling fans on two computers, as well as other instrumentation such as the oscilloscope and streak camera controllers; laser water cooling pumps on the floor near the bench; and a vacuum pump near the bench firmly attached to the helitran sample mount. As much as possible, simple tests were taken to determine which caused the greatest temporal dispersion to the data by turning various components off and on and

observing changes in beam quality. Although the tests were not quantitative, all items mentioned were observed to contribute qualitatively to the temporal dispersion.

Temporal Dispersion from Time Range Settings and Slit Widths.

Time range settings of the voltage sweep also impact the temporal resolution of the streak camera. As mentioned in “Streak Camera Operation,” time range settings in the streak camera change the amplitude of the sinusoidal sweep voltage across the photo-electrons resulting in a change to the overall time range of the temporal image area. Because the number of pixels is fixed, pixels will collect electrons from larger time periods with longer sweep times, thus degrading the minimal resolution for a given setting. Manufacturer’s test report give a minimum full-width half maximum (FWHM) temporal resolution of 16.93 pixels [27]. The ratio of this number to the total number of pixels (1016) was used to define the temporal resolution relative to the imaging screen. The absolute temporal resolutions in Table 1 were calculated by multiplying this number with the time ranges also given in Table 1. These values are labeled “Min Res” in Figure 33.

Additionally, the horizontal spectrometer slit widths impact temporal resolution for the same reason the vertical spectrometer slit widths effect the spectral resolution. Because the approximately 250 fs laser pulse is below the minimum resolution of the streak camera, the device measures the signal at the minimum resolution for the given conditions. To test these two effects, the spectrometer was set to the laser wavelength (about 2734 Å), and measurements of the laser pulse were made at various spectrometer slit widths and all time ranges, as shown in Figure 33.

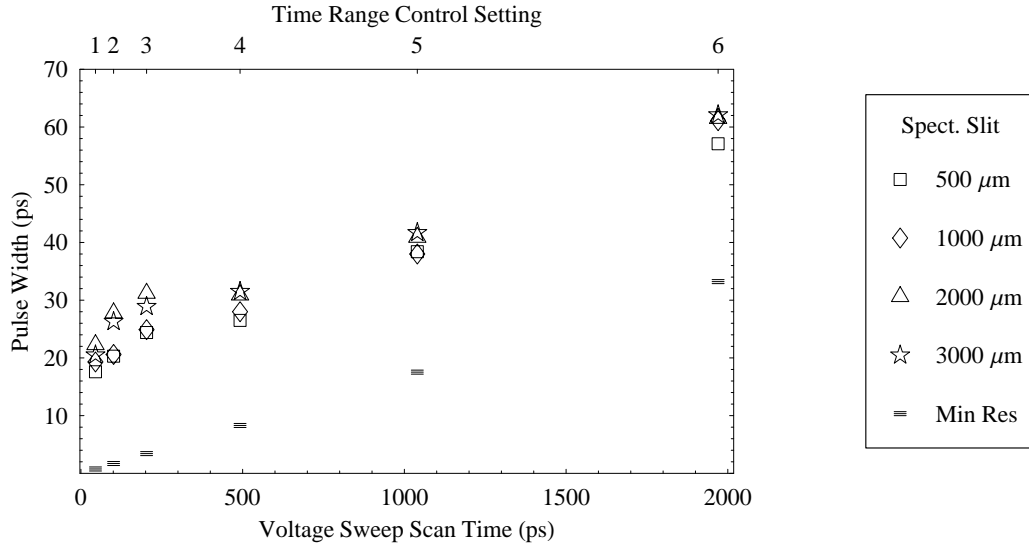


Figure 33. Temporal Resolution Dependence on Sweep Time Range and Spectrometer Slit Width. Streak Camera slit was 60 μm ; spectrometer slit widths are given in the legend. The “Min Res” data set is the set of minimum possible temporal resolution for each time range control setting, as discussed. The x-axes match Table 1.

Temporal resolution is defined by a full-width half maximum (FWHM) of a pulse equaling 16.93 pixels. Minimum resolution was calculated by the ratio of this FWHM value to the 1016 pixels multiplied by the full time range of a sweep (Table 1). The data in Figure 33 show that the time range settings follow this formula, but with some offset. This offset represents a temporal dispersion in the data, discussed later. Changing the spectrometer entrance slit widths (“Spect. Slit” in the legend) should not change the temporal resolution. This value does not significantly impact the longer sweeps although, interestingly, the shorter sweeps suffer from decreased spectrometer slit width which is contrary to the trend shown in the spectral resolution data (Figure 31).

Figure 33 shows three important things. First, as expected, the spectrometer slit width does not significantly impact the temporal resolution of the streak camera, except

at short time ranges. Second, because temporal resolution comes from a fraction of total pixels, sweeping longer time ranges increases the minimum amount of time which can be temporally resolved (thereby decreasing temporal resolution). Third, streak camera slit width impacts temporal resolution.

Figure 34 illustrates the problem with streak images of the laser pulse which were collected separately from Figure 33. The streak camera slit width was set to 1 mm, and rather than imaging the temporal profile of a laser pulse (left y-axes), the camera directly imaged the physical width of the slit instead (right y-axes). This shows that narrow slit width (less than 50 μm with 30 μm ideal) is critical for achieving instrument-limited temporal resolution such as in Figure 35 which shows a temporally resolved image of a laser pulse with a streak camera slit of 40 μm .

Collecting data with a narrow slit width ($\leq 50 \mu\text{m}$), as shown in Figure 35, was only accomplished when the horizontal alignment between the streak camera and the spectrometer was nearly perfect. The difficulty of this task was compounded by the fact that both the spectrometer and streak camera do not rest directly on the table. They are raised to the plane of the helitran, suspended from above. Unfortunately, the lab jacks supporting the streak camera only had coarse adjustments which tended to relax over time. As a result, consistently high temporal resolution was not possible, although short term results were obtained. Figure 36 shows how resolution depends upon the streak camera slit width in the vertical (and hence temporal) axis of the streak signal.

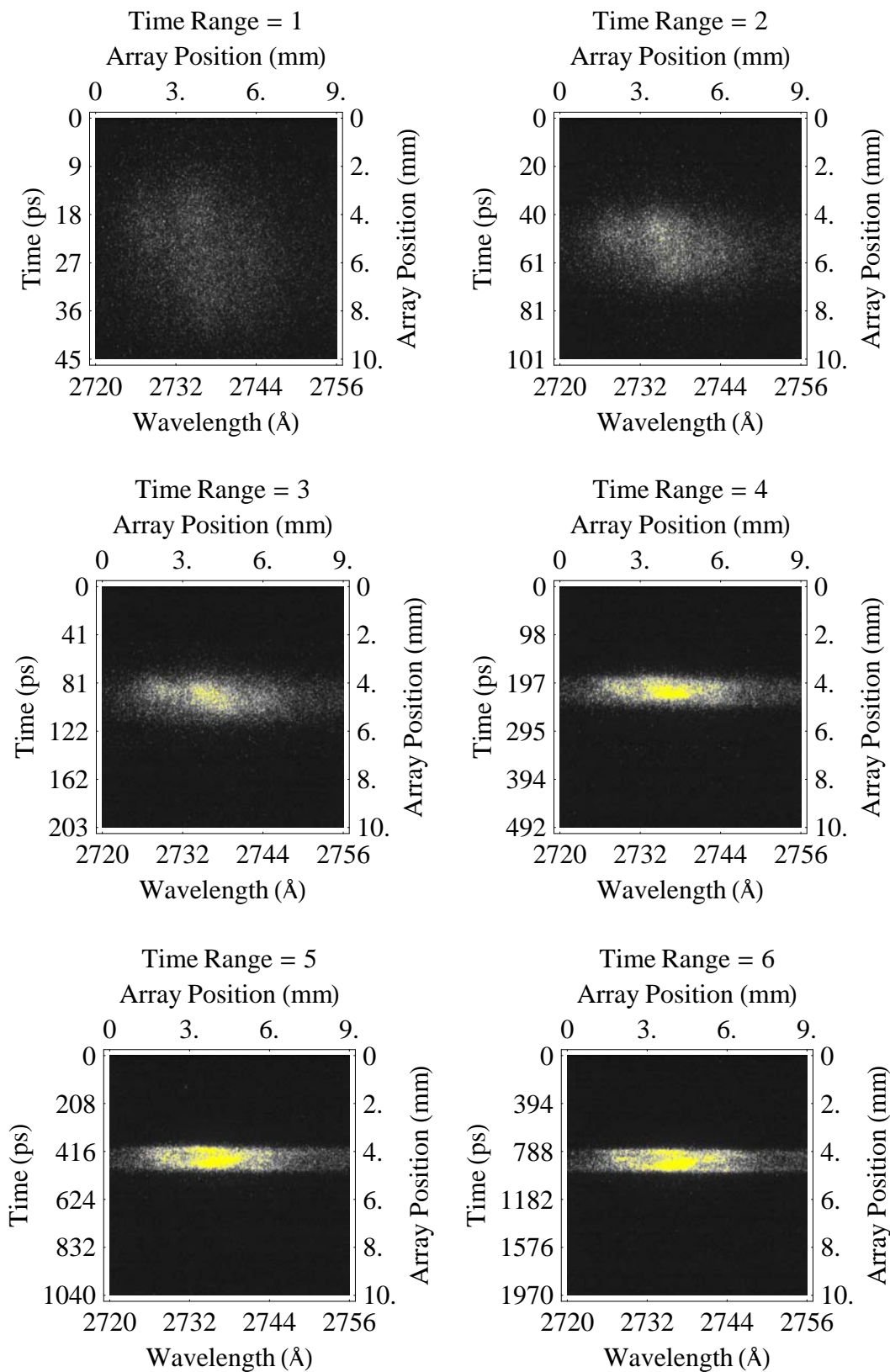


Figure 34. Poorly Resolved Laser Pulses on All Temporal Time Ranges.

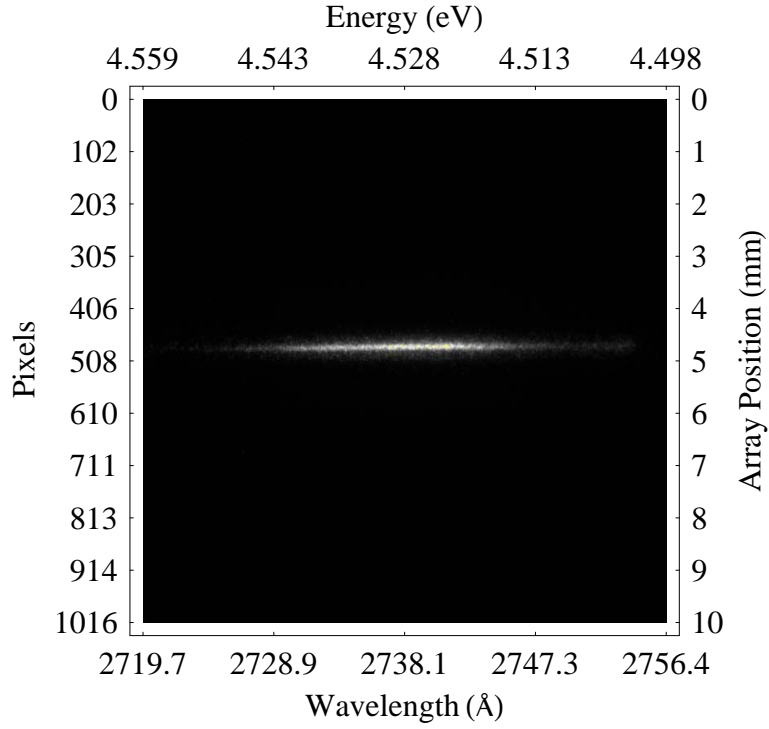


Figure 35. TRPL of a Laser Pulse with Low Temporal Dispersion. Streak camera slit was set to 40 μ m.

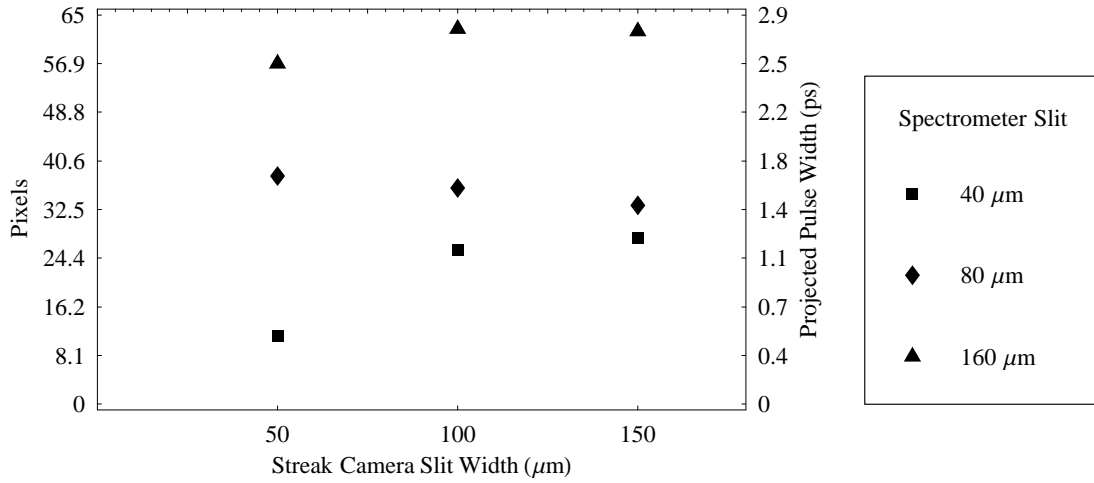


Figure 36. Pulse Widths of Laser Pulses Measured on the Streak Camera. Streak Camera was in focus mode (no sweep voltage) so data were measured in pixels (left y-axis) and projected into pulse widths based on a 45-ps sweep period (right y-axis). In focus mode with a 10- μ m slit, vertical resolution is seven pixels [27].

Semiconductor Data

Most of the time available for experimentation was expended troubleshooting the temporal issues as noted. However, enough time was available to demonstrate the experiment's proof of concept and to affirm the system's utility for further research.

Time-Integrated Photoluminescence.

Before TRPL was performed, a baseline time-integrated PL was accomplished to compare results with other efforts. This was accomplished using the PMT as described in the introduction to the "Experimental Setup" chapter. Samples were tested at room temperature (294 K, Figure 37) and low temperatures (5 K, Figure 38). No features were evident below 3500 Å, and running PL beyond the 5000 Å saturated the PMT with the diffraction double of the laser. The spectrum in Figure 37 exhibits band-edge structure of the crystal, and the spectrum in Figure 38 exhibits many carrier recombination species.

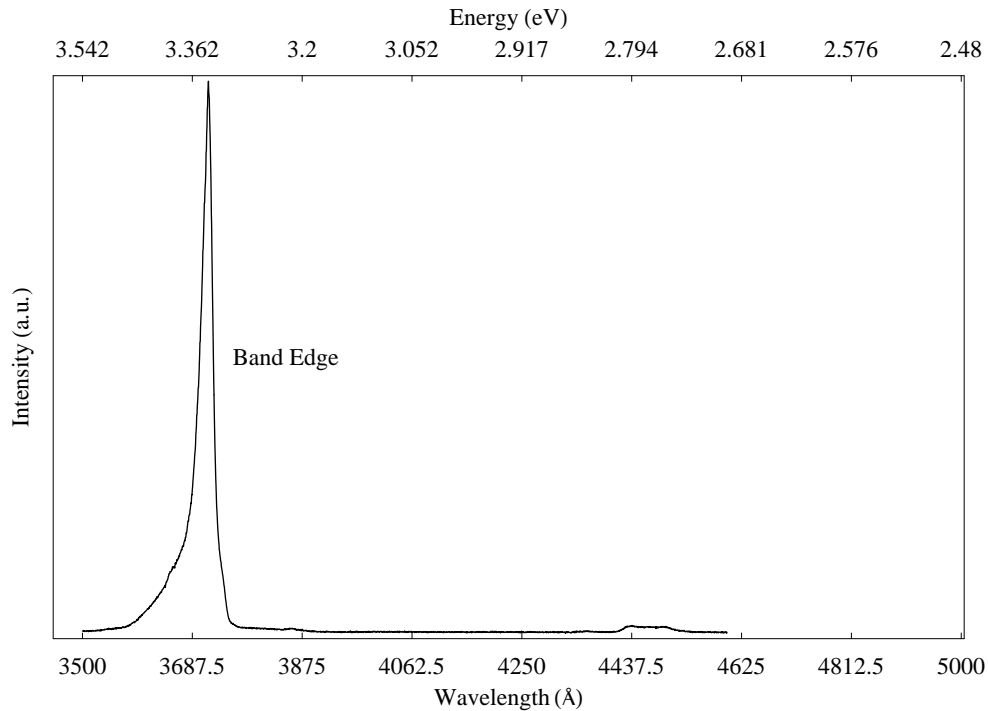


Figure 37. Time-Integrated Photoluminescence of GaN at 294 K.

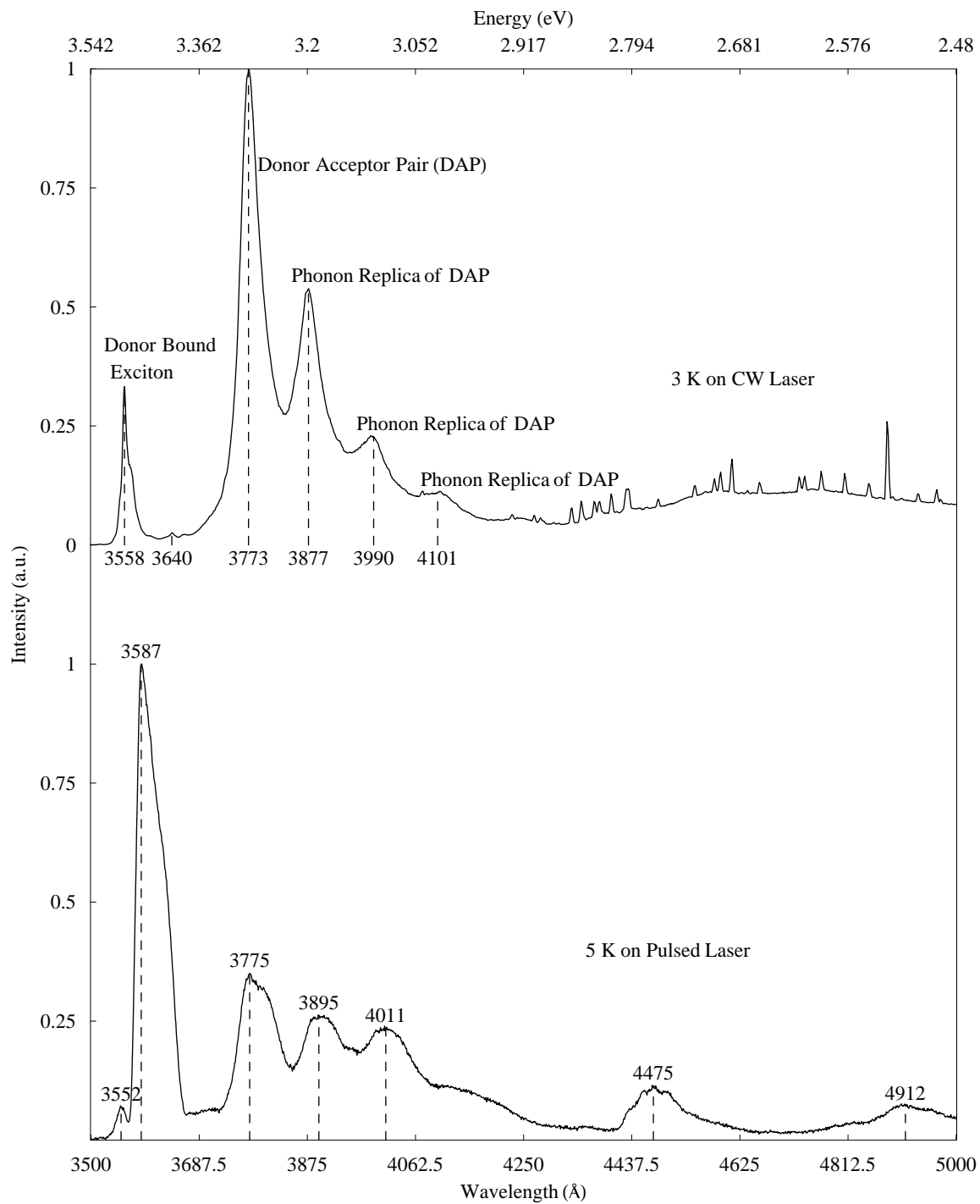


Figure 38. Time-Integrated Photoluminescence of GaN at 5 K.

The bottom plot is original, and the top plot is the same sample at 3 K using a CW laser [33]. Phonon replicas occur when photon energy is reduced by phonon quanta

Time-Resolved Photoluminescence.

Although temporal dispersion plagued TRPL data collection, some data were collected to prove successful experimental setup within the limits of the temporal noise. No temporal signal above the noise was detected at room temperature; however, the longer lifetimes of PL species at 5 K exceeded the noise and a small temporal data set was collected.

Streak Analyses.

Streaks exhibiting expected behavior occurred between 3500 and 3600 Å at 5 K. A sample of data collected is shown in Figure 39.

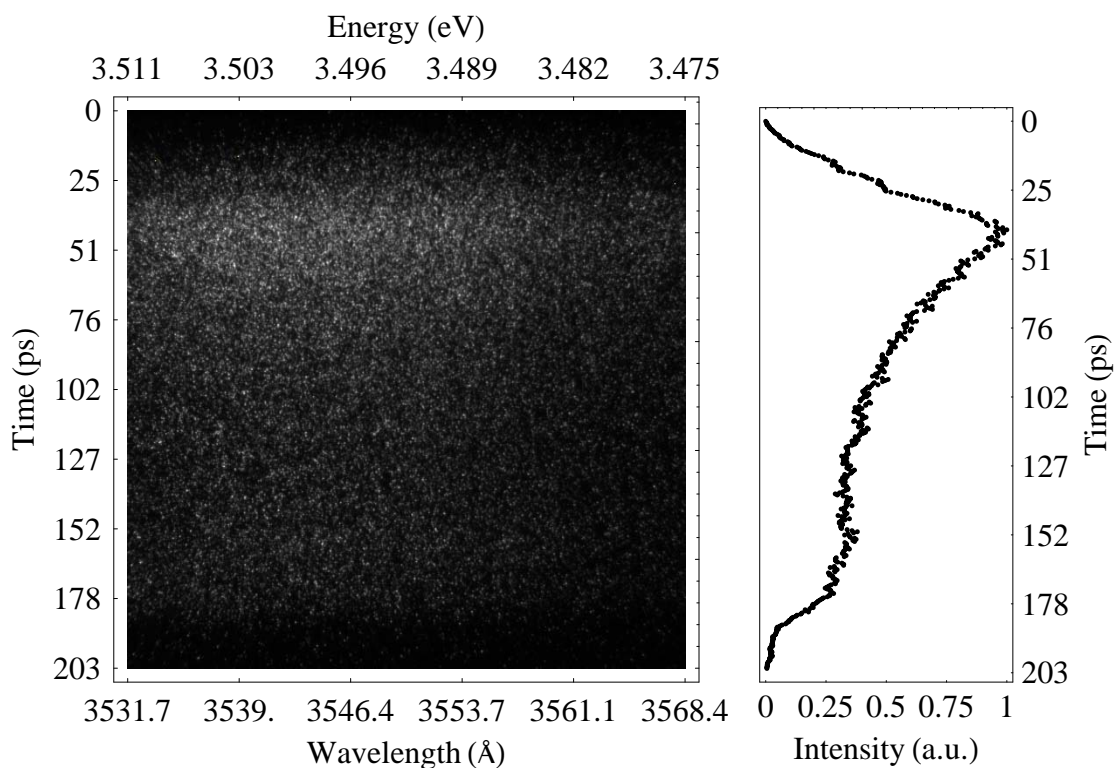


Figure 39. Streak Image of GaN at 5K.

The image on the left has been spectrally mapped as described earlier, and the image on the right is a spectrally-integrated temporal plot. The two time axes are identical.

As shown in Table 2, the spectrum on the streak camera is very narrow. To understand what is showing spectrally, it is useful to draw lines on the spectrum representing the screen capture. This spectral “window” is shown in Figure 40 and, along with Figure 39, satisfies Research Objective 2, “Collect PL and TRPL spectral data (check for self-consistency) and temporal TRPL data from carrier recombination events.” Temporal analysis of the streak requires more discussion.

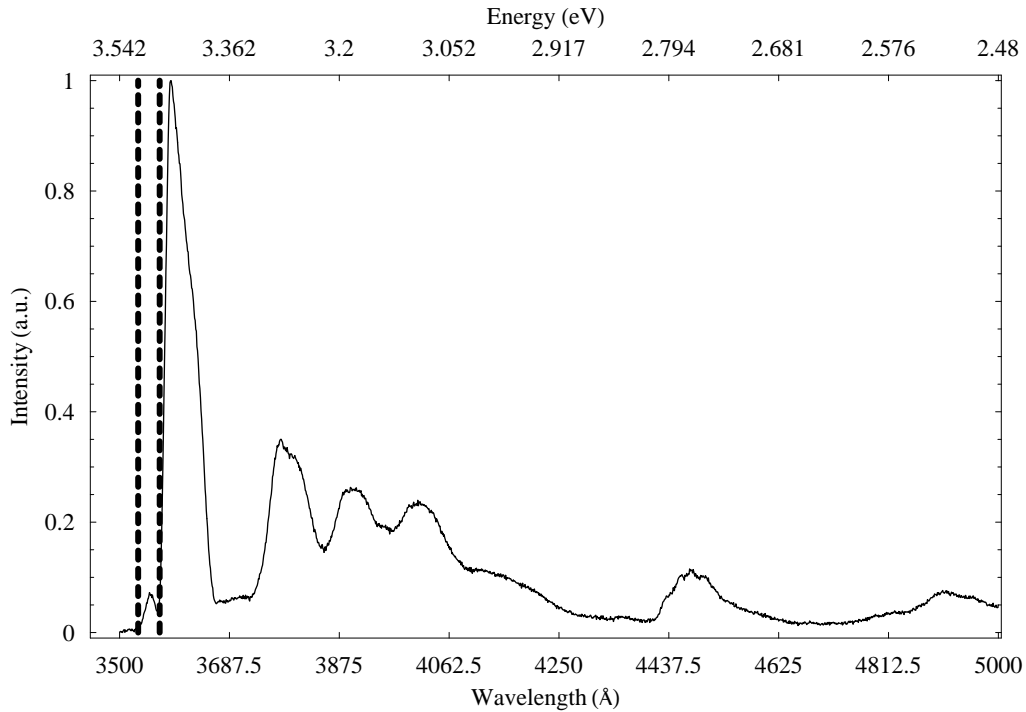


Figure 40. Streak Camera Spectrum of GaN at 5 K Bounded on the PL Spectrum. The dashed line indicates the streak camera’s spectral width (Table 2), and the solid line is the PL spectrum obtained from the PMT.

Three temporal profiles were collected as shown in Figure 41. The first two (“Set 1” and “Set 2”) came from the peak around 3552 Å. The third (“Set 3”) came from the peak around 3587 Å. Of the two data sets from the peak at 3552 Å, Set 1 appeared to come from an upward sweep on the sweep voltage—contrary to the customary downward

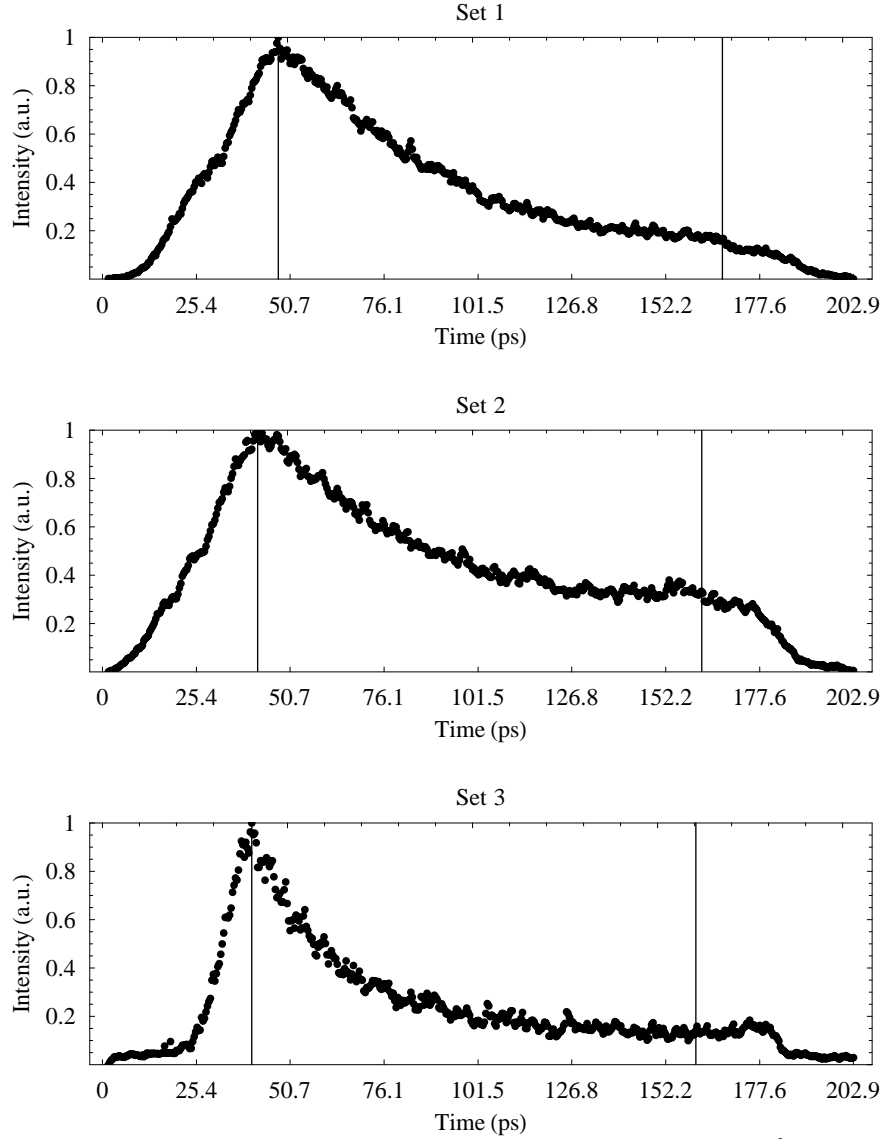


Figure 41. Temporal Profiles of TRPL Collected around 3552 Å.

sweep. When the temporal axis was reversed, it matched Set 2 very closely. This phenomenon is discussed in more detail in “Multiple Streaks”.

The sweep delay changes the temporal location of the image, so the “zero” value in Figure 41 is arbitrary. The cause of the sharp drops beyond 175 ps is not known. Because of known temporal jitter problems, the reliability of this data is suspicious.

Furthermore, the features evaluated were thought to be donor-bound excitons, and because the theory resulting in Equation (39) applies to band-to-band recombination, it is not known if it even applies to these events. Nevertheless, data were analyzed in accordance with both procedures outlined in the “Carrier Recombination Rate” section.

The selected data above were fit to the double exponential (Equation (46)) by least-squares error which yielded the plot shown in Figure 42. Parameters for the curve fits are shown in Table 3 where the σ -values are standard deviation and τ is defined by the standard definition:

$$\frac{1}{\tau} = \frac{1}{\tau_1} + \frac{1}{\tau_2}. \quad (50)$$

From Table 3, lifetimes for the peak at 3552 Å are 43.2 ± 1.6 ps, using mean values are weighted by the nonuniform uncertainties [34:59], and lifetimes for the peak at 3587 Å are 16.8 ± 3.4 ps.

Table 3. Decay Times from Least-Squares Error Fit to a Double Exponential.

<i>Set</i>	<i>A</i> (<i>a.u.</i>)	σA (<i>a.u.</i>)	τ_1 (<i>ps</i>)	$\sigma\tau_1$ (<i>ps</i>)	<i>B</i> (<i>a.u.</i>)	σB (<i>a.u.</i>)	τ_2 (<i>ps</i>)	$\sigma\tau_2$ (<i>ps</i>)	τ	$\Sigma\tau$
1	0.92	0.11	45.5	5.6	0.09	0.01	10^{16}	10^{15}	45.5	5.6
2	0.77	0.13	40.0	6.7	0.27	0.04	10^{16}	10^{15}	40.0	6.7
3	0.71	0.14	18.6	3.8	0.25	0.05	169	34.3	16.8	3.4

Alternatively, data were also fit by least squares error to Equation (45). The equation was modified with the addition of initial luminescence ($k_4 = L'(t_0)$) which is linked to initial excess carrier density in Equation (42). This $L'(t_0)$ value was not

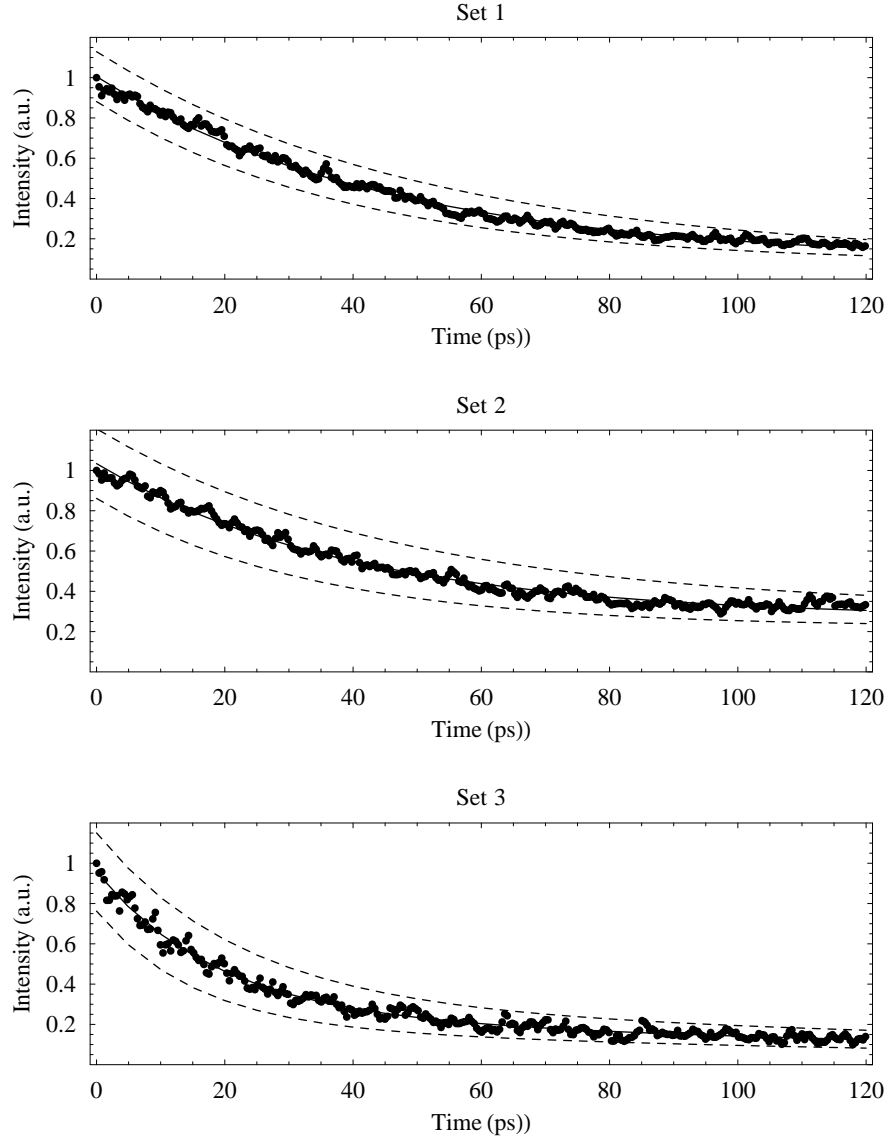


Figure 42. Double Exponential Curve Fits to Luminescence Intensity Decay Data. Dashed lines are error in curve fit.

measured because streak camera signal strength varies not only by initial excess carrier density, but also by micro-channel plate gain settings on the camera. Data were normalized for simplicity. Parameters resulting from the fit are shown in Table 4, and plots showing the data fit are shown in Figure 43. For Table 4, the units depend on which recombination parameter is represented, but the time portion is in picoseconds.

Table 4. Parameters for Least Squares Error Fit to Luminescence Intensity Decay Data.

<i>Set</i>	<i>k1</i>	$\sigma k1$	<i>k2</i>	$\sigma k2$	<i>k3</i>	$\sigma k3$	<i>k4</i>	$\sigma k4$
1	-0.020	0.002	9.4E-4	0.00009	2.2E-5	2E-6	1.0	0.1
2	-0.018	0.002	8.0E-4	0.0001	2.6E-5	3E-6	1.0	0.1
3	-0.050	0.01	7.0E-3	0.001	-2.8E-4	6E-5	1.0	0.2

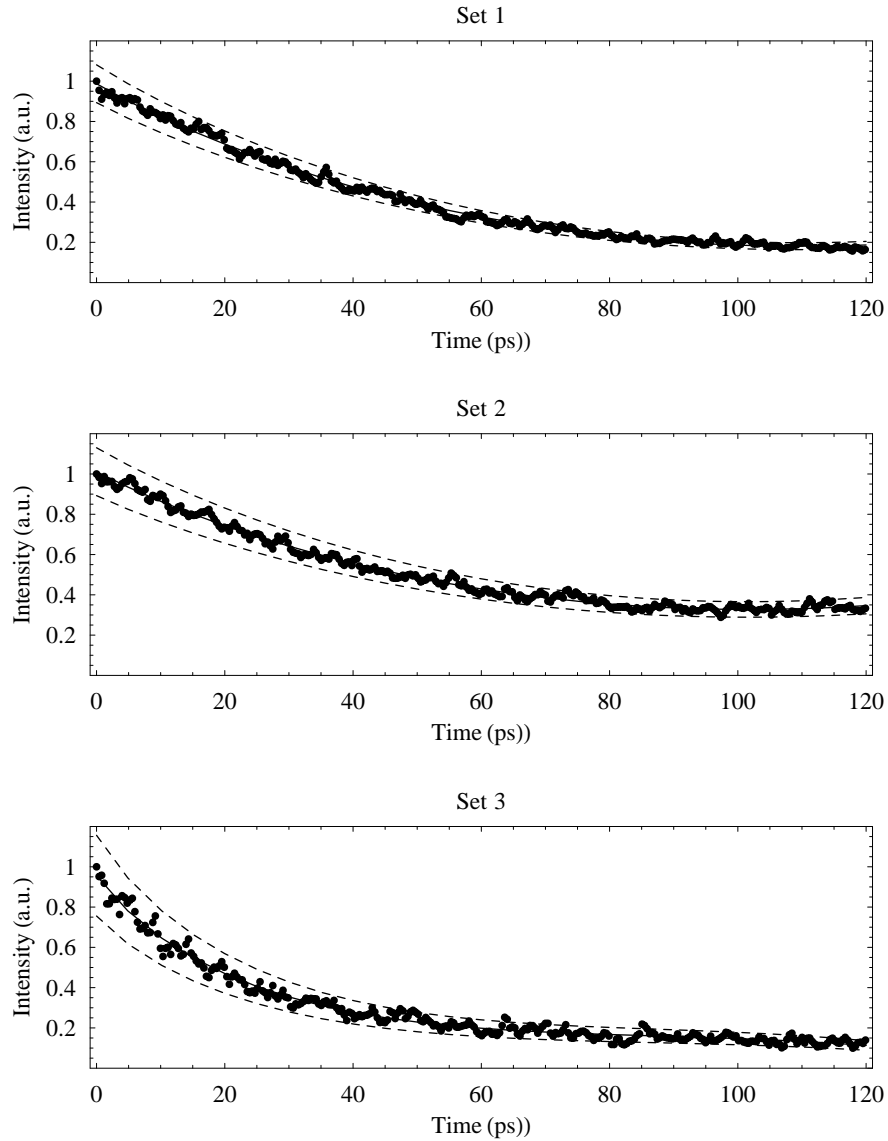


Figure 43. Least Squares Error Fit to Luminescence Intensity Decay Data.

Perhaps more importantly, the values for A_{SRH} , B_{Rad} , C_{Aug} as calculated from $k1$, $k2$ and $k3$ (Equation (45)) are included in Table 5 where the mean values are again weighted by the nonuniform uncertainties [34:59]. Here, the time portion of the units have been converted into seconds. Because data were normalized, the $k4$ parameter was not used. Data are parameterized in terms of η because its value was not measured. Because η is an efficiency ($0 < \eta < 1$), these values can be considered the largest possible, and the real values must be smaller. Nevertheless, the large uncertainty not quantified in the calculation casts doubt on the reliability of these numbers.

Table 5. Values for A_{SRH} , B_{Rad} , C_{Aug} .

<i>Set</i>	A_{SRH} (s^{-1})	σA_{SRH} (s^{-1})	B_{Rad} (cm^3/s)	σB_{Rad} (cm^3/s)	C_{Aug} (cm^6/s)	σC_{Aug} (cm^6/s)
1	-9.8E9	9.3E8	$8.9E17\eta$	$1.7E17\eta$	$2.0E25\eta^2$	$5.6E24\eta^2$
2	-8.8E9	1.0E9	$6.4E17\eta$	$1.5E17\eta$	$1.7E25\eta^2$	$6.0E24\eta^2$
Mean of 1 & 2	-9.3E9	4.9E8	$7.5E17\eta$	$8.0E16\eta$	$1.8E25\eta^2$	$2.9E24\eta^2$
3	-2.5E10	5.2E9	$4.9E19\eta$	$2.0E19\eta$	$-1.4E28\eta^2$	$-8.6E27\eta^2$

Multiple Streaks.

Another important utility of the streak camera is the ability to compare the timing of two separate radiative events. Knowledge of the relative time between events may provide insight into the physics of how the two events relate. The two events discussed in “Streak Analyses” are a pair of such events. Quantitative results regarding the time between the two events were not obtained.

As shown in the time-integrated PL spectrum in Figure 40, the spectral region isolated for TRPL study includes two photoluminescent peaks. Although it was not surprising to find two peaks at different times, varying the delay caused the two images to move in different directions as shown in the following sequence of streak images in Figure 44. Understanding the sweep mechanism proved helpful in figuring out why the peaks moved opposite each other.

As mentioned in “Streak Camera Operation”, the voltage sweep across the electron beam in the streak camera exhibits sinusoidal form matched to the repetition period of the laser (13.2 ns). As a result, photoelectrons from one PL event were swept down while photoelectrons from the other PL event were swept up. For both of them to be visible on the same screen, the time between them must be about half the period of the sweep or about 6 or 7 ns. Because the events clearly differ in time by more than the longest sweep the camera makes (1.97 ns, Table 1), firm numbers correlating the two events were not possible without devising a new method.

Comparing the TRPL of Figure 44 to the PL of Figure 40 raises another concern. Clearly in the PL spectrum, the feature on the right exhibits a stronger intensity while in the TRPL spectrum, the feature on the left exhibits stronger intensity. An experimentalist may wonder if perhaps this apparent contradiction is because the wavelength axes are inverted (from high to low). However, streak camera performance, as well as comparison of mercury lamp features (Figure 30), contradicts the idea. No other explanation is offered.

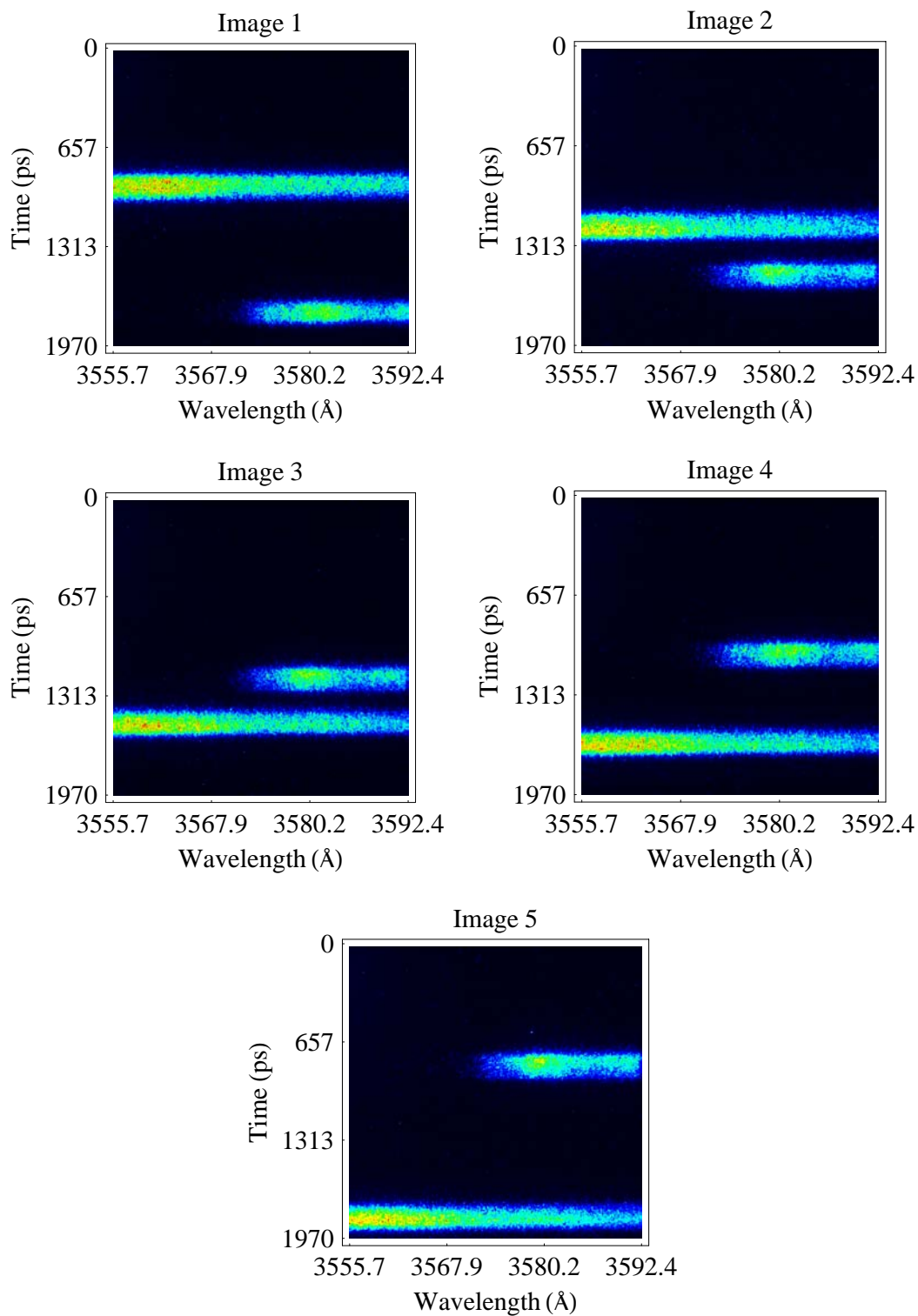


Figure 44. Sequential TRPL Streaks of GaN at 5 K with Varied Sweep Delay. The temporal axes shown are arbitrarily referenced to zero.

V. Conclusions and Recommendations

Conclusions about Experimental Setup

Experimental Objective 1, “Design, build and test an operational laboratory experiment which uses a streak camera to perform TRPL,” was satisfied. The experimental setup is nearly ready to begin collecting quality temporally-resolved data. In particular, the streak camera is now a proven instrument and combined with both the new system setup and calibration data in this document, will prove useful for future measurements.

The spectrometer was calibrated and found to be accurate within 0.7 \AA . While performing as a monochromator, the instrument performed as expected when considering trade-offs between resolution and signal strength that depend on entrance and exit slit widths. The streak camera spectral characteristics were also characterized, and the spectral dispersion of the spectrometer was mapped to the image pixels of the streak camera. On average, the screen width was found to capture 36.6 \AA of spectrum.

Temporal performance of the streak camera was characterized. Problems with temporal dispersion and poor temporal data were identified, and some of these issues were resolved. In particular, the trade-offs between streak camera slit width and temporal resolution were analyzed. It was discovered that temporal resolution is above measurement range unless the slit is at most $50 \text{ }\mu\text{m}$ in width with a desired value of $30 \text{ }\mu\text{m}$. It was difficult to collect light at this slit width because of a horizontal misalignment between the spectrometer and the streak camera. Coarsely adjustable lab

jacks supporting the streak camera were found to cause this problem which should be solved by replacing the jacks having high precision height control.

Vibration was also identified as a major cause of temporal dispersion. Vibration sources include water pumps, vacuum pumps, electronics and failure to dampen table vibrations adequately. All these problems are resolvable by isolating the source from the sample and measurement system.

Conclusions about Samples

Data collected satisfy Experimental Objective 2, “Collect PL and TRPL spectral data (check for self-consistency) and temporal TRPL data from carrier recombination events.” Time-integrated photoluminescence was performed on a GaN sample at room temperature and at 5 K. Room temperature data showed classic band-edge structure (Figure 37) and cooled sample data (Figure 38) showed consistency with other data. Data were consistent with previous measurements for the same samples using a CW laser instead of the pulsed laser of this experiment.

Time-resolved photoluminescence (TRPL) was also performed on the GaN sample at two different spectral features thought to be donor-bound excitons: one at 3552 Å and another at 3587 Å. These data were fit using least squares error to a double exponential equation (Equation (46)) resulting in lifetime, $\tau = 43.2 \pm 1.6$ ps for the peak at 3552 Å and are $\tau = 16.8 \pm 3.4$ ps for the peak at 3587 Å. The uncertainty represents sum of squares error in data fit. Known, but unquantified, temporal noise was not included in the uncertainty.

The same luminescence intensity decay data were also fit by least squares error to the carrier recombination rate equation mapped to luminescence intensity (Equation (45)). From the resulting fit parameters, Shockley-Read-Hall (A), Radiative (B) and Auger (C) coefficients were calculated. These values were parameterized, in terms of η , the experimental efficiency in measuring photoluminescent intensity. Time did not permit measurement of this value. Values for the peak at 3552 Å are

$$A = -9.3 \times 10^9 \pm 4.9 \times 10^8 \text{ s}^{-1}, B = 7.5 \times 10^{17} \eta \pm 8.0 \times 10^{16} \eta \text{ cm}^3/\text{s} \text{ and}$$

$$C = 1.8 \times 10^{25} \eta^2 \pm 2.9 \times 10^{24} \eta^2 \text{ cm}^6/\text{s}, \text{ and values for the peak at 3587 Å are}$$

$$A = -2.5 \times 10^{10} \pm 5.2 \times 10^9 \text{ s}^{-1}, B = 4.9 \times 10^{19} \eta \pm 2.0 \times 10^{19} \eta \text{ cm}^3/\text{s} \text{ and}$$

$$C = -1.4 \times 10^{28} \eta^2 \pm 8.6 \times 10^{27} \eta^2 \text{ cm}^6/\text{s}. \text{ Negative values in the fit are troubling, but no}$$

explanation is offered. These results satisfy Experimental Objective 3, “Calculate radiative, Shockley-Read-Hall and Auger coefficients for GaN samples,” but the uncertainty of the data is high.

Recommendations

Major Recommendations to Laboratory Setup.

The most challenging problems to the experiment involved vibration and alignment. Making the first two of the following changes should permit data collection as precise as the temporal resolution limit of the streak camera. Another problem was not being able to measure the power, which the third major recommendation will solve.

Mount Streak Camera on High Precision Jacks.

Adequate temporal resolution depends on very precise horizontal alignment between the streak camera and the spectrometer. Controls on the jacks currently

supporting the streak camera are too coarse to permit sufficiently precise alignment. Resources should be prioritized to this issue.

Arrest Vibration.

System vibrations introduce a large amount of noise in the temporal data, again prohibiting high-resolution measurements. The following actions should eliminate the noise to permit successful measurements in accordance with experimental Objective 3.

Use Turbo Pump with High Strength Valve.

Vibrations from the vacuum pump are coupled directly into the sample holder. Vacuum pumping is critical for cryogenic cooling, but a turbo pump with a high strength valve could be turned off during experimentation thus eliminating operating noises.

Mount Helitran on Translatable Stage.

First of all, the helitran is currently suspended from the upper lab bench which also houses computers and power supplies. Vibrations from the cooling fans in the electronics are coupled directly into the helitran before they are damped by the main bench air-damped suspension. The helitran has four threaded holes in the bottom which would permit bolting to a plate. This plate could be designed to also include a truss which supports the bulky instrument.

Secondly, the helitran is fixed in place. Up to four samples may be mounted on the cold finger, but to illuminate a different sample, the beam must be moved. This movement disrupts the entire optical alignment after the sample, and this disruption has two detracting elements. The first effect is the time required to realign optics, namely the off-axis parabolic mirror which requires precise alignment and orientation in six degrees of freedom. The second effect is much more severe: the resulting realignment prohibits

consistency between PL measurements because each time new alignment occurs, a different fraction of the emitted light enters the analysis system, changing the value for η . This difference in light is an unknown which prohibits inferring relative strengths between photoluminescent features of different samples or even on the same sample taken at different times (which can be important if the beam is moved between temperature changes). The helitrans plate discussed above could be mounted to a three-axis translation stage.

Brace Upper Bench to the Floor.

The upper laboratory bench above the main work-space supports the many electronics which operate the laboratory equipment. Cooling fans in these devices cause vibrations which the supports couple directly into the main lab bench. Bracing this bench on the floor instead of the main lab bench will eliminate these vibrations.

Purchase a Wavelength-Specific Power Meter.

Beam power and pulse width were unknown until the very end of the experiment because a power meter was not available. This measurement should be taken daily in data collection due to its critical importance in the curve-fitting equation; therefore, a power meter dedicated to the laboratory is essential. The upconverted wavelength of the THG lies outside the spectral response of the currently dedicated equipment (beam wavelength is shorter). A power meter which responds at both 270 nm and 405 nm would be most useful as this would include the frequency doubled line, as well as the tripled.

Beam pulse width is useful to determine the temporal response of the streak camera, but comparing an unknown with an assumed value is not as useful as comparing

an unknown with a measured value. An autocorrelator whose sensor has a spectral response within range of the upconverted laser beam could perform this measurement. Although the power meter could perform this measurement on a constructed interferometer, this effort would distract from the experimental focus.

Minor Recommendations to Laboratory Setup.

Although successful measurement may be possible without the following recommendation, they will add value to the experimentation process.

Consider a Shorter Spectrometer.

The current experimental setup includes a 0.5-meter spectrometer and the streak camera, and the streak camera images a spectrum of approximately 37 \AA or 3.7 nm . Although this provides the ability to closely examine one phenomenon, it may be too close to simultaneously examine two separate events which occur in spectral proximity. Because of temporal jitter and drift, the experimenter is denied a temporal reference as the spectrum is shifted (via the spectrometer) from one location to another. Subsequently, the experimenter may not draw accurate conclusions about the relative time between the events. This recommendation will need reconsideration when the vibration and temporal resolution issues are resolved.

Replace Argon Ion Laser with a Diode-Pumped Device.

The argon ion laser is a workhorse, but it is often an unreliable pumping source and takes an extensive amount of warm-up time. Power variations ripple instability throughout the experiment, and at times, this particular laser spontaneously ceased lasing altogether. A suitable alternative is a neodymium: vanadate laser pumped by diode lasers

and frequency doubled to match the titanium: sapphire transitions. It is a turn-key operation and more stable.

Replace Household Cling Wrap Beam Splitter with Appropriate Material.

The S1 optic in Figure 16 is household cling wrap. It functions adequately, but it splits off so much power that the beam has to be attenuated to prevent photodiode saturation and subsequent trigger failure. This power could be saved for illuminating the sample if an optical component replaced this improvised beamsplitter. A flat optic which is anti-reflective coated near the titanium: sapphire primary wavelength would supply enough power for the photodiode to trigger the streak camera sweep.

Recommendations for Further Research

As a result of the research completed in characterizing the experimental setup (and pending recommendations to the laboratory setup in the previous section), the following actions will greatly strengthen reliability of the data collection process..

Correlate Streak Camera Intensity with Beam Intensity.

As noted in “Streak Analyses” section, streak camera signal strength varies not only by luminescence intensity, but also by the gain settings on its micro-channel plate. Achieving good fit to Equation (34) requires knowledge of both these values which, in turn, requires further research to complete a data map.

Determine Experimental Efficiency, η .

Table 5 and Equation (45) show the importance of knowing the experimental efficiency in collecting laser luminescence. Before proceeding with further semiconductor TRPL, this factor should be measured at various settings to determine its value with a high degree of certainty.

Summary

Characterization of carrier recombination is important for understanding and improving the performance of semiconductor devices. The carrier recombination rate equation can be matched to time-intensity profiles of luminous emissions from a stimulated semiconductor using time resolved photoluminescence (TRPL). An ultra-short pulse laser such as a mode-locked titanium: sapphire laser can stimulate semiconductors, and a streak camera can perform ultra-fast TRPL. This was done for the first time at AFIT using GaN samples cooled to 5 K.

The streak camera was calibrated to a known spectral image, and temporal measurements were also performed. The streak camera was calibrated to a known spectral image, and temporal measurements were also performed for peaks at 3552 Å and 3587 Å. Lifetime measurements were found to be $\tau = 43.2 \pm 1.6$ ps for the peak at 3552 Å and are $\tau = 16.8 \pm 3.4$ ps for the peak at 3587 Å. Parameterized Shockley-Read-Hall, Radiative and Auger coefficients were found for the peak at 3552 Å are $A = -9.3 \times 10^9 \pm 4.9 \times 10^8 \text{ s}^{-1}$, $B = 7.5 \times 10^{17} \eta \pm 8.0 \times 10^{16} \eta \text{ cm}^3/\text{s}$ and $C = 1.8 \times 10^{25} \eta^2 \pm 2.9 \times 10^{24} \eta^2 \text{ cm}^6/\text{s}$, and values for the peak at 3587 Å are $A = -2.5 \times 10^{10} \pm 5.2 \times 10^9 \text{ s}^{-1}$, $B = 4.9 \times 10^{19} \eta \pm 2.0 \times 10^{19} \eta \text{ cm}^3/\text{s}$ and $C = -1.4 \times 10^{28} \eta^2 \pm 8.6 \times 10^{27} \eta^2 \text{ cm}^6/\text{s}$, in terms of the experimental efficiency parameter, η , which was not measured. Problems plagued temporal resolution including mechanical vibrations and imprecise alignment between the spectrometer and the streak camera. Resolution of these problems should increase measurement precision which yields data that gives insight into atomic mechanisms of wide band gap semiconductors.

Appendix A: Calibration of Streak Camera Wavelength

Overview

The streak camera does not measure wavelength directly. Instead it measures a horizontal distance which can be related to a spectrum if calibrated. Calibration requires clear reference points which must provide information on the spectral difference between features as well as their spectral location. An excellent example of this is the mercury doublet at 3125.7 and 3131.7Å [35]. These provide the scale (difference between the peaks) and reference (absolute wavelength) necessary to map the pixels of the streak camera into calibrated wavelength information. To calibrate the streak camera, execute the following procedure.

Calibration Procedure

- Place mercury lamp in front of spectrometer in darkened room
- Collect photoluminescence data on two peaks such as the 3125.7 and 3131.7Å peaks — it may be helpful to center your data set between the peaks
- Set spectrometer wavelength to the center of the two peaks and change output to the streak camera
- Collect photoluminescence data on the streak camera (time resolution is not needed) — again it may be helpful to center your data set between the peaks

Analysis

- Normalize the y -values to the maximum peak (this ensures both PMT and streak camera data may be shown on the same graph)
 - Subtract the noise floor (minimum y -value) from all y -values
 - Divide all y -values by the maximum y -value
- Scale the x -values of the streak camera from *pixels* to *wavelength*
 - Find the positions within the data array for the x -value of the 2 maxima (x_1 and x_2) for each graph
 - Find the difference, Δ , between the two peaks on each graph. For reference, let the PMT data be x (in wavelength) and the streak camera data be x' (in pixels)
 - Scale the streak camera data so x' (pixels) $\rightarrow x' \Delta x / \Delta x'$ (wavelength) thus $\Delta x' / \Delta x$ gives you the *pixel-to-wavelength* ratio
 - Find the screen width of the streak camera in units of wavelength; this is the last x -value of the scaled data
- Shift the x -values
 - Consider the relative x -positions of the same peak on both graphs. Shift the streak camera data by the difference between these two peaks so that $x' \Rightarrow x' - (x_1' - x_1)$. This aligns the positions
- Plot the results to confirm proper procedure

Bibliography

- [1] Verdeyen, Joseph T., *Laser Electronics*, 3rd ed. Prentice Hall, Upper Saddle River NJ, 1995.
- [2] Hecht, Eugene. *Optics*, 4th ed. Addison Wesley, San Francisco, 2002.
- [3] McKelvey, John P. *Solid State Physics for Engineering and Materials Science*, Krieger Publishing Company, Malabar, FL, 1993.
- [4] Sze, S.M. *Semiconductor Devices: Physics and Technology* (2nd Ed). John Wiley and Sons Inc, New York, 2002.
- [5] Pankove, Jacques I. *Optical Processes in Semiconductors*. Dover Publications, Inc. New York, 1971.
- [6] Weeks, David. Private Conversation (12 August 2004).
- [7] Battacharya, Pallab, *Semiconductor Optoelectronic Devices*, Prentice Hall, New Jersey, 1997.
- [8] Bougrov V., Levinshtein M.E., Rumyantsev S.L., Zubrilov A., in *Properties of Advanced Semiconductor Materials GaN, AlN, InN, BN, SiC, SiGe*. Eds. Levinshtein M.E., Rumyantsev S.L., Shur M.S., John Wiley & Sons, Inc., New York, 2001, 1-30.
- [9] Maruska, H.P and Tietjen, J.J., *Applied Physics Letters*, 15 (1969) 327.
- [10] Ramirez-Flores, G., H. Navarro-Contreras, A. Lastrae-Martinez, R.C. Powell, J.E. Greene, "Temperature-Dependent Optical Band Gap of the Metastable Zinc-Blende Structure Beta-GaN", *Physical Review B* 50(12) (1994), 8433-8438.
- [11] Shankar, R., *Principles of Quantum Mechanics* (2nd Ed). Kluwer Academic/Plenum Publishers, New York, 1994.
- [12] Wolfe, Charles M; Holonyak, Nick Jr and Stillman, Gregory E. *Physical Properties of Semiconductors*. Prentice Hall, New Jersey 1989.
- [13] Mroziewicz, Bohdan; Bugajski, Maciej and Nakwaski, Wlodzimierz. *Physics of Semiconductor Lasers*. Translated by Jolanta Krauze, Polish Scientific Publishers, Warszawa, 1991.
- [14] Shockely, W and Read, R.T. Jr. "Statistics of the Recombinations of Holes and Electrons", *Physical Review*, Volume 87, Number 5, 1952.

- [15] Beattie, A.R. and Landsberg, P.T., “Auger Effect in Semiconductors” Proceedings of the Royal Society of London, Volume 249, 1959.
- [16] Johnson, Peter M. *Deviation of Time-Resolved Luminescence Dynamics in MWIR Semiconductor Materials from Carrier Recombination Theory Predictions*. Thesis, Air Force Institute of Technology, 2002.
- [17] Sun, C.K. and others. “Optical investigations of the dynamic behavior of GaSb/GaAs quantum dots”, American Institute of Physics, 1996. As seen at www.ece.ucsb.edu/uoeg/research/publications/papers/sun96apl.pdf on Jan 6, 2005.
- [18] Gorski, Steven M. and others. “Time-resolved photoluminescence spectra of mid-infrared quantum-well lasers,” Solid State and Diode Laser Technology Review 2002 Technical Digest, (Directed Energy Professional Society, 2002), p. MIR7.
- [19] Cooley, W.T. and others. Appl. Phys. Lett. 73, 20 (1998).
- [20] Ferguson, E.G. and others. “Ultra-fast spectroscopy of optically pumped mid-infrared semiconductor laser materials and devices,” presented at the American Physical Society March 2003 Meeting (X8 4), 3-7 March 2003, Austin, TX.
- [21] Gorski, Steven M. *Carrier Dynamics in Mid-Infrared Quantum Well Lasers Using Time-Resolved Photoluminescence*. MS thesis, AFIT/GAP/ENP/02M-01. School of Engineering Physics, Air Force Institute of Technology (AU), Wright-Patterson AFB OH, March 2002.
- [22] Johnson, Peter M. and others. “Deviation of carrier dynamics in MWIR photonic structures from theoretical predictions,” Proceedings of the 2004 Great Lakes Photonics Symposium, (SPIE, 2004).
- [23] Johnson, Peter M. and others. “Excitation- and structure-dependence of recombination mechanisms in antimony-based MWIR photonic devices,” presented at the American Physical Society March 2004 Meeting (B10 9) held on 22-26 March 2004 in Montreal, Canada.
- [24] Ultra-fast Harmonic Generation System, Model 5-050, Technical Manual, Inrad, Northvale, NJ, 1998.
- [25] Hamamatsu Web Page. “What is a Streak Camera?” <http://usa.hamamatsu.com/sys-streak/operating/default.htm>. Accessed 25 October 2002.

- [26] Cieslik, William C and Kaufmann, Kenneth J., "Detection of Ultra-fast Phenomena with Streak Cameras and PMT," *Proceedings of SPIE Vol. 4280, Ultra-fast Phenomena in Semiconductors V*, 2001.
- [27] Hamamatsu. "Test Report" Streak Camera C6860-21, Serial Number 630013. Tested by M. Wada and approved by T. Matsumota. 11 March 2004.
- [28] Hamamatsu Web Page. "Femtosecond Streak Camera Specifications." <http://usa.hamamatsu.com/assets/pdf/hpspdf/Femtosecond.pdf?GLBSESSID=589b816f18c140f0c52c7a9cf28ae7e2>. Accessed 14 June 2004.
- [29] Hamamatsu Web Page. "Products." <http://usa.hamamatsu.com/en/products/system-division/ultra-fast/streak-systems/c6860.php?&group=1&GLBSESSID=589b816f18c140f0c52c7a9cf28ae7e2#>. Accessed 14 June 2004.
- [30] E-mail from Treiber, A. at Hamamatsu Corporation (November 12, 2004).
- [31] "Streak Camera Instruction Manual C6860: Operation Guide", Hamamatsu Photonics K.K. Sunayama-Cho, Japan. Not dated.
- [32] Marciniak, Michael, Class Lecture, Optical Engineering 651, Optical Diagnostics Laboratory, Air Force Institute of Technology, Wright-Patterson AFB OH, Summer Quarter 2004.
- [33] Fellows, James A., *Electrical Activation Studies of Ion Implanted Gallium Nitride*. Dissertation, Air Force Institute of Technology, 2002.
- [34] Bevington, Philip R. and Robinson, D. Keith, *Data Reduction and Error Analysis for the Physical Sciences*, 2nd Ed. McGraw-Hill, Inc. New York. 1992.
- [35] Oriel Corporation. "Typical Spectra of Oriel Spectral Lamps." Stamford, CT. Not dated.

Vita

Captain Thomas R. Jost graduated from Superior Senior High School in Superior, Wisconsin. He entered undergraduate studies at the United States Air Force Academy the same year where he was commissioned upon graduation four years later.

His first assignment was to Brooks Air Force Base where he served in the Air Force Research Laboratory as a program manager and in 311th Air Base Group as the Executive Officer. He then developed Air Force policy for directed energy weapons as the Chief Weapons Analyst at the Air Force Safety Center at Kirtland Air Force Base.

While at Kirtland Air Force Base he was selected to attend the Air Force Institute of Technology Graduate School of Engineering and Management. Upon graduation, he will be assigned to Detachment 15 of the Air Force Research Laboratory in Hawaii at the Air Force Maui Optical and Supercomputing Site.

REPORT DOCUMENTATION PAGE				Form Approved OMB No. 074-0188	
<p>The public reporting burden for this collection of information is estimated to average 1 hour per response, including the time for reviewing instructions, searching existing data sources, gathering and maintaining the data needed, and completing and reviewing the collection of information. Send comments regarding this burden estimate or any other aspect of the collection of information, including suggestions for reducing this burden to Department of Defense, Washington Headquarters Services, Directorate for Information Operations and Reports (0704-0188), 1215 Jefferson Davis Highway, Suite 1204, Arlington, VA 22202-4302. Respondents should be aware that notwithstanding any other provision of law, no person shall be subject to a penalty for failing to comply with a collection of information if it does not display a currently valid OMB control number.</p> <p>PLEASE DO NOT RETURN YOUR FORM TO THE ABOVE ADDRESS.</p>					
1. REPORT DATE (DD-MM-YYYY) 01-03-2005		2. REPORT TYPE Master's Thesis		3. DATES COVERED (From - To) Jun 2004 - Mar 2005	
4. TITLE AND SUBTITLE LIMITATIONS IN TIME RESOLVED PHOTOLUMINESCENCE OF GALLIUM NITRIDE USING A STREAK CAMERA				5a. CONTRACT NUMBER	
				5b. GRANT NUMBER	
				5c. PROGRAM ELEMENT NUMBER	
6. AUTHOR(S) Jost, Thomas R., Captain, USAF				5d. PROJECT NUMBER	
				5e. TASK NUMBER	
				5f. WORK UNIT NUMBER	
7. PERFORMING ORGANIZATION NAMES(S) AND ADDRESS(S) Air Force Institute of Technology Graduate School of Engineering and Management (AFIT/EN) 2950 Hobson Way WPAFB OH 45433-7765				8. PERFORMING ORGANIZATION REPORT NUMBER AFIT/GAP/ENP/05-04	
9. SPONSORING/MONITORING AGENCY NAME(S) AND ADDRESS(ES) AFRL/AFOSR Attn: Dr. Todd Steiner 4015 Wilson Blvd. Arlington VA 22203-1954 (703) 696-7314				10. SPONSOR/MONITOR'S ACRONYM(S)	
				11. SPONSOR/MONITOR'S REPORT NUMBER(S)	
12. DISTRIBUTION/AVAILABILITY STATEMENT APPROVED FOR PUBLIC RELEASE; DISTRIBUTION UNLIMITED.					
13. SUPPLEMENTARY NOTES					
14. ABSTRACT Semiconductor performance is often characterized in terms of the rate at which its carrier recombination processes occur. Carrier recombination, including radiative, and Shockley-Read-Hall and Auger (both nonradiative), occurs at ultra-fast times in the picosecond or femtosecond regimes. A device which can measure both spectral data and temporal phenomena at this speed is the streak camera. The capability to do time-resolved spectroscopy of wide band gap semiconductors using a streak camera has been established at AFIT for the first time. Time resolved photoluminescence (TRPL) from samples of gallium nitride were measured at temperatures of 5 K over spectral bands of 36.6 Å and temporal ranges of 45 to 1970 ps, both instrument-limited. TRPL features at 3552 Å and 3587 Å were studied giving decay lifetimes of 43.2 ± 1.6 ps and 16.8 ± 3.4 ps, respectively. Shockley-Read-Hall, Radiative and Auger coefficients were found but parameterized in terms of experimental efficiency, η , which was not measured. These values, determined using a least-squares-error fit of the carrier recombination rate equation to collected data, are $-9.3 \times 10^9 \pm 4.9 \times 10^8 \text{ s}^{-1}$, $7.5 \times 10^{17} \eta \pm 8.0 \times 10^{16} \eta \text{ cm}^3/\text{s}$, and $1.8 \times 10^{25} \eta^2 \pm 2.9 \times 10^{24} \eta^2 \text{ cm}^6/\text{s}$ respectively, for the first peak and $-2.5 \times 10^{10} \pm 5.2 \times 10^9 \text{ s}^{-1}$, $4.9 \times 10^{19} \eta \pm 2.0 \times 10^{19} \eta \text{ cm}^3/\text{s}$ and $-1.4 \times 10^{28} \eta^2 \pm 8.6 \times 10^{27} \eta^2 \text{ cm}^6/\text{s}$ for the second peak. Since alignment of the streak camera has not yet been optimized, large but unquantified uncertainty in these results exists. Isolating vibrations and improving streak camera alignment should reduce the uncertainty and permit data collection temporally resolved at hundreds of femtoseconds.					
15. SUBJECT TERMS Semiconductors, Wide Band Gap Semiconductors, Gallium Nitride, Carrier Recombination, Photoluminescence Carrier Recombination Rate, Carrier Lifetime, Radiative Lifetime, Auger Coefficient, Shockley-Read-Hall Coefficient, Streak Camera, Time Integrated Photoluminescence, Time Resolved Photoluminescence					
16. SECURITY CLASSIFICATION OF:			17. LIMITATION OF ABSTRACT	18. NUMBER OF PAGES	19a. NAME OF RESPONSIBLE PERSON
REPORT	ABSTRACT	c. THIS PAGE			Dr. Michael A. Marciniak, (ENP)
U	U	U	UU	102	19b. TELEPHONE NUMBER (Include area code) (937) 255-6565, ext 4529; e-mail: Michael.Marciniak@afit.edu

Standard Form 298 (Rev. 8-98)
Prescribed by ANSI Std. Z39-18